Composite Structures 255 (2021) 112964

Contents lists available at ScienceDirect

Composite Structures

journal homepage: www.elsevier.com/locate/compstruct

# Nonlinear behavior analysis of electrostatically actuated multilayer anisotropic microplates with residual stress

Zhikang Li [a,b,c,d,e], Libo Zhao [a,b,c,*], Jie Li [a,b,c], Yihe Zhao [a,b,c], Tingzhong Xu [a,b,c], Zichen Liu [a,b,c], Guoxi Luo [a,b,c], Shiming Zhang [d,e], Kaiming Hu [g], Tyler Hoffman [d,e], Shahid Saghir [f], Dejiang Lu [a,b,c], Wenming Zhang [g,*], Zhuangde Jiang [a,b,c]

[a] State Key Laboratory for Manufacturing Systems Engineering, Xi'an Jiaotong University, Xi'an, Shaanxi 710049, China
[b] International Joint Laboratory for Micro/Nano Manufacturing and Measurement Technologies, Xi'an Jiaotong University, Xi'an, Shaanxi 710049, China
[c] School of Mechanical Engineering, Xi'an Jiaotong University, Xi'an, Shaanxi 710049, China
[d] Department of Bioengineering, University of California-Los Angeles, Los Angeles, CA 90095, USA
[e] California NanoSystems Institute, University of California-Los Angeles, Los Angeles, CA 90095, USA
[f] Department of Mechanical Engineering, University of Management and Technology, Sialkot Campus 21-A, Small Industrial Estate, Shahabpura Road, Sialkot, Pakistan
[g] State Key Laboratory of Mechanical System and Vibration, School of Mechanical Engineering, Shanghai Jiao Tong University, Shanghai 200240, China

ARTICLE INFO

*Keywords:*
Electrostatically actuated multilayer microplates
Material anisotropy
Residual stress
Hydrostatic pressure
Scale effects
Nonlinear mechanical behaviors
Closed-form expressions

ABSTRACT

Electrostatically actuated microplates with multilayer and material anisotropy properties, are widely employed in microelectromechanical systems. However, previous theories rarely consider the aforementioned properties simultaneously, hindering their widespread application. This paper proposes a general theoretical model for electrostatically actuated rectangular multilayer anisotropic microplates subjected to residual stress and hydrostatic pressure by combining the classical laminated thin plate theory, Galerkin method and a partial expansion approach for nonlinear electrostatic force. This model enables successful establishment of closed-form expressions for the main mechanical behaviors, e.g. the pull-in voltage, static deflection, and resonant frequency. Validation of these expressions, using finite element method simulations and experimental results, shows significant improvement in the analysis accuracy (15 times higher) compared to those theories neglecting the material anisotropy, as well as excellent applicability across a wide range of DC voltages and dimensions. Additionally, the influences of electrostatic softening effects and scale effects on the theories are also discussed.

## 1. Introduction

Micro- and nano-sensors and actuators have been in high demand for various industrial applications because of their advantages of small size, high sensitivity, superior capacities of batch fabrication and system integration [1–6]. As one of the building blocks of microelectromechanical systems (MEMS) devices, electrostatically actuated microplates have been widely used in resonators, micro-pumps, micro-switches, etc. [7–11]. Generally, an electrostatically actuated microplate-based device composes of two microplates, in which one microplate is suspended in parallel over the other fully fixed one. The nonlinear mechanical behaviors of the suspended microplate under electrostatic force, such as static deflection, resonant frequency and pull-in voltage, determine the device performance [12–19]. In capacitive micromachined ultrasonic transducers (CMUTs) for instance, the DC voltage determines the electromechanical coupling coefficient by changing its static deflection [20]. For resonant biochemical sensors, the DC voltage influences the detection sensitivity by changing their fundamental resonant frequencies [21]. Besides, the pull-in voltage determines the applicable range of the DC voltage. Understanding these performance-related static and dynamic behaviors is important for the optimization and operation of microplate-based electrostatic devices, significantly decreasing the time and cost for device development.

Towards this end, numerous studies have been done to investigate the aforementioned mechanical behaviors [8,22,23]. Owing to the inherent nonlinearity of the existing electrostatic force, the partial differential equation governing the deflection and vibration is difficult to be solved analytically using previously developed methods [24]. Therefore, some researchers developed step-by-step lin-

* Corresponding authors at: State Key Laboratory for Manufacturing Systems Engineering, Xi'an Jiaotong University, Xi'an, Shaanxi 710049, China (L. Zhao).
*E-mail addresses:* libozhao@xjtu.edu.cn (L. Zhao), wenmingz@sjtu.edu.cn (W. Zhang).

https://doi.org/10.1016/j.compstruct.2020.112964
Received 11 May 2020; Revised 28 August 2020; Accepted 9 September 2020
Available online 14 September 2020

earization methods and used different iterative methods to obtain convergent solutions [25–27]. A large number of other researchers utilized the Galerkin method to develop reduced-order models for this problem, which was demonstrated to be an effective approach [28]. For example, Caruntu and Oyervides [29] developed a reduced-order model based on the classical thin plate theory to study the effects of DC voltage and air damping on the resonant frequency of clamped circular microplates. To predict the large deflection of microplates under electrostatic force, reduced-order models considering the middle-plane stretching effects were established [30]. For example, Vogl and Nayfeh [31], and Zhao et al. [24] established reduced-order models based von Karmán thin plate theory. Sajadi et al. [32,33] established a reduced-order model by combining the von Karmán thin plate theory and an energy approach. Further, Casimir force, thermal stress, and initial deformation were introduced into the reduced-order models [34–37]. More recently, reduced-order models based on the modified couple stress theory were developed to simulate size effects [38–41]. Besides, many other approaches, such as the finite element difference method, shooting method and displacement iteration pull-in extraction algorithm have also been developed for the analysis of the nonlinear mechanical behaviors [42–44].

Although the aforementioned work has made significant progress, substantial efforts are still required for more efficient and accurate modeling of the aforementioned nonlinear behaviors. Firstly, the material anisotropy of microplates are rarely taken into account, which results in significant analysis errors, reported to be 25% [45,46]. Secondly, most of the developed theoretical models apply to single-layer microplates, limiting their application for multilayer microplates which are more frequently employed in MEMS. Thirdly, most previous methods are a semi-analytical approach, and the solutions are evaluated numerically, the accuracy of which fluctuates with the iterative methods and voltage step size used [47]. Towards these drawbacks, Maurizio Porfiri [48] and our group [49–51] developed closed-form expressions for clamped circular and rectangular microplates. However, these expressions were applied to single-layer isotropic microplates. Zand and Ahmadian [42] studied the vibration behavior of the multilayer isotropic microplates by combining the finite element and finite difference methods. Cour et al. [52] investigated the deflection and pull-in voltage of two layers of anisotropic microplates using lumped parameters. However, both aforementioned studies were based on semi-analytical methods and no closed-form expressions were proposed. Therefore, to date, a general theoretical model and closed-form expressions, which can simultaneously take into account the multilayer and material anisotropy properties, have not been established.

Herein, we develop a general theoretical model for electrostatically actuated rectangular microplates with both properties of arbitrary multilayers and material anisotropy considered, subjected to residual stress and pressure using the classical laminated thin plate (CLTP) theory, the Galerkin method and a partial expansion method to approximate electrostatic force. Based on this model, closed-form expressions for the static deflection, pull-in voltage and resonant frequency are established successfully. These closed-form expressions are validated by finite element method (FEM) simulation-based parametric study and experimental results, showing that: 1) the accuracy of the developed expressions is significantly improved compared with that of the theories based on isotropic material properties; 2) these expressions have the robustness and high analysis accuracy across a wide range of DC voltages (up to 96% of pull-in voltages) and dimensions (thickness-to-width ratio of 1/100–1/20), even when the deflection of the microplate reaches its thickness. Additionally, we further investigate the influences of electrostatic softening effect and scale effects on the analysis accuracy of the developed closed-form expressions.

## 2. Problem formulation

### 2.1. Stress–strain relationships

The schematic of an electrostatically actuated rectangular microplate with $n$ layers is shown in Fig. 1. Each layer, as well as the whole plate, is assumed to be anisotropic and thin. Each layer has the same length of $2a$ and width of $2b$, but different mechanical properties and dielectric constants. The bottom microplate is fixed in parallel with respect to the top multilayer microplate with a distance of $d_0$, between which the gap is assumed to be air or vacuum. The top microplate with its all edges clamped can vibrate under the co-action of DC and AC voltages. The CLTP theory is used for the analysis of the nonlinear mechanical behaviors of the top multilayer microplate [53,54].

Theoretical modeling of electrostatically actuated multilayer anisotropic microplates starts with the relationship between the stress and strain of linear elastic materials, which can be described by Hooke's law as :

$$\tilde{\sigma}_{pq}^{k} = \tilde{C}_{pqlm}^{k}\tilde{\varepsilon}_{pq}^{k} \tag{1}$$

where $\tilde{\sigma}_{pq}^{k}$ and $\tilde{\varepsilon}_{pq}^{k}$ represent stress and strain of the $k$th layer, respectively; $\tilde{C}_{pqlm}^{k}$ represents the stiffness and the subscripts $p,q,l,m = 1, 2, 3$. Eq. (1) is an extremely complicated matrix because $\tilde{C}_{pqlm}^{k}$ is a fourth rank tensor, representing 81 elastic constants. However, given the symmetry property of the stresses and strains, as well as the elastic and symmetric characteristics of the materials in most general cases of anisotropy, Eq. (1) can be drastically simplified into Eq. (2) with 21 independent elastic constants.

$$\begin{bmatrix} \tilde{\sigma}_1^k \\ \tilde{\sigma}_2^k \\ \tilde{\sigma}_3^k \\ \tilde{\sigma}_4^k \\ \tilde{\sigma}_5^k \\ \tilde{\sigma}_6^k \end{bmatrix} = \begin{bmatrix} \tilde{C}_{11}^k & \tilde{C}_{12}^k & \tilde{C}_{13}^k & \tilde{C}_{14}^k & \tilde{C}_{15}^k & \tilde{C}_{16}^k \\ \tilde{C}_{21}^k & \tilde{C}_{22}^k & \tilde{C}_{23}^k & \tilde{C}_{24}^k & \tilde{C}_{25}^k & \tilde{C}_{26}^k \\ \tilde{C}_{31}^k & \tilde{C}_{32}^k & \tilde{C}_{33}^k & \tilde{C}_{34}^k & \tilde{C}_{35}^k & \tilde{C}_{36}^k \\ \tilde{C}_{41}^k & \tilde{C}_{42}^k & \tilde{C}_{43}^k & \tilde{C}_{44}^k & \tilde{C}_{45}^k & \tilde{C}_{46}^k \\ \tilde{C}_{51}^k & \tilde{C}_{52}^k & \tilde{C}_{53}^k & \tilde{C}_{54}^k & \tilde{C}_{55}^k & \tilde{C}_{56}^k \\ \tilde{C}_{61}^k & \tilde{C}_{62}^k & \tilde{C}_{63}^k & \tilde{C}_{64}^k & \tilde{C}_{65}^k & \tilde{C}_{66}^k \end{bmatrix} \begin{bmatrix} \tilde{\varepsilon}_1^k \\ \tilde{\varepsilon}_2^k \\ \tilde{\varepsilon}_3^k \\ \tilde{\varepsilon}_4^k \\ \tilde{\varepsilon}_5^k \\ \tilde{\varepsilon}_6^k \end{bmatrix} \tag{2}$$

where $\tilde{\sigma}_i^k$, $\tilde{\varepsilon}_i^k$ and $\tilde{C}^k{}_{pqlm}$ are the condensed notations for $\tilde{\sigma}_{pq}^k$, $\tilde{\varepsilon}_{pq}$ and $\tilde{C}_{pqkl}$, respectively, where $i, j = 1, 2,\ldots 6$ [54]. In the coordinate system, stress matrix $\tilde{\sigma}^k$ for the $k$th layer can be rewritten as:

$$\tilde{\sigma}^k = \begin{bmatrix} \tilde{\sigma}_1^k & \tilde{\sigma}_2^k & \tilde{\sigma}_3^k & \tilde{\sigma}_4^k & \tilde{\sigma}_5^k & \tilde{\sigma}_6^k \end{bmatrix}^{\mathrm{T}} = \begin{bmatrix} \tilde{\sigma}_x^k & \tilde{\sigma}_y^k & \tilde{\sigma}_z^k & \tilde{\tau}_{yz}^k & \tilde{\tau}_{xz}^k & \tilde{\tau}_{xy}^k \end{bmatrix}^{\mathrm{T}} \tag{3}$$

and the corresponding strain matrix $\tilde{\varepsilon}^k$ can be expressed as:

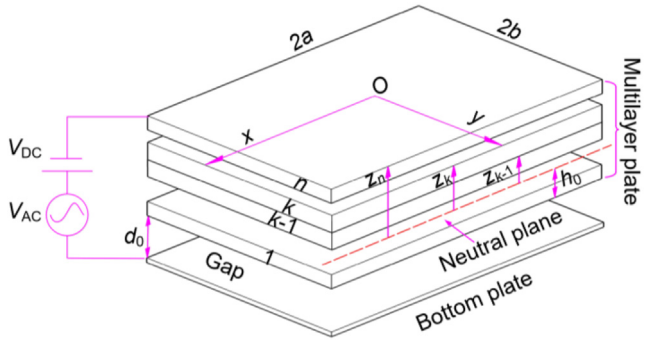


**Fig. 1.** Schematic illustration of electrostatically actuated rectangular multilayer anisotropic microplates.

$$\tilde{\varepsilon}^k = \begin{bmatrix} \tilde{\varepsilon}_1^k & \tilde{\varepsilon}_2^k & \tilde{\varepsilon}_3^k & \tilde{\varepsilon}_4^k & \tilde{\varepsilon}_5^k & \tilde{\varepsilon}_6^k \end{bmatrix}^{\mathrm{T}} = \begin{bmatrix} \tilde{\varepsilon}_x^k & \tilde{\varepsilon}_y^k & \tilde{\varepsilon}_z^k & \tilde{\gamma}_{yz}^k & \tilde{\gamma}_{xz}^k & \tilde{\gamma}_{xy}^k \end{bmatrix}^{\mathrm{T}} \quad (4)$$

where $\tilde{\sigma}_x$ ($\tilde{\varepsilon}_x$), $\tilde{\sigma}_y$ ($\tilde{\varepsilon}_y$) and $\tilde{\sigma}_z$ ($\tilde{\varepsilon}_z$) are the principal stresses (principal strains) in the $x$, $y$ and $z$ axes aligned with the principal material directions, respectively; $\tilde{\tau}_{yz}$ ($\tilde{\gamma}_{yz}$), $\tilde{\tau}_{xz}$ ($\tilde{\gamma}_{xz}$) and $\tilde{\tau}_{xy}$ ($\tilde{\gamma}_{xy}$) are the shear stresses (shear strains) in yz, xz and xy planes, respectively. As silicon, with orthotropic material properties, is the most commonly used material in MEMS sensors and actuators [45], Eq. (2) can be further simplified as:

$$\begin{bmatrix} \tilde{\sigma}_x^k \\ \tilde{\sigma}_y^k \\ \tilde{\sigma}_z^k \\ \tilde{\tau}_{yz}^k \\ \tilde{\tau}_{xz}^k \\ \tilde{\tau}_{xy}^k \end{bmatrix} = \begin{bmatrix} \tilde{C}_{11}^k & \tilde{C}_{12}^k & \tilde{C}_{13}^k & 0 & 0 & 0 \\ \tilde{C}_{21}^k & \tilde{C}_{22}^k & \tilde{C}_{23}^k & 0 & 0 & 0 \\ \tilde{C}_{31}^k & \tilde{C}_{32}^k & \tilde{C}_{33}^k & 0 & 0 & 0 \\ 0 & 0 & 0 & \tilde{C}_{44}^k & 0 & 0 \\ 0 & 0 & 0 & 0 & \tilde{C}_{55}^k & 0 \\ 0 & 0 & 0 & 0 & 0 & \tilde{C}_{66}^k \end{bmatrix} \begin{bmatrix} \tilde{\varepsilon}_x^k \\ \tilde{\varepsilon}_y^k \\ \tilde{\varepsilon}_z^k \\ \tilde{\gamma}_{yz}^k \\ \tilde{\gamma}_{xz}^k \\ \tilde{\gamma}_{xy}^k \end{bmatrix} \quad (5)$$

The transverse shear and normal strains in Eq. (5) can be ignored, that is, $\tilde{\gamma}_{xz} = \tilde{\gamma}_{yz} = 0$ and $\tilde{\varepsilon}_z = 0$, because of the use of the CLTP theory. Therefore, the stress–strain relationship at a plane stress state can be derived from Eq. (5) as:

$$\begin{bmatrix} \tilde{\sigma}_x^k \\ \tilde{\sigma}_y^k \\ \tilde{\tau}_{xy}^k \end{bmatrix} = \begin{bmatrix} \tilde{Q}_{11}^k & \tilde{Q}_{12}^k & 0 \\ \tilde{Q}_{12}^k & \tilde{Q}_{22}^k & 0 \\ 0 & 0 & \tilde{Q}_{66}^k \end{bmatrix} \begin{bmatrix} \tilde{\varepsilon}_x^k \\ \tilde{\varepsilon}_y^k \\ \tilde{\gamma}_{xy}^k \end{bmatrix} \quad (6)$$

where, $\tilde{\boldsymbol{Q}}^{\boldsymbol{k}}$ is a reduced stiffness matrix for the stiffness matrix in Eq. (5), and each entry $\tilde{Q}_{ij}^k$ can be expressed in engineering elastic constants as:

$$\begin{aligned} \tilde{Q}_{11}^k &= \frac{E_x^k}{1-\mu_{xy}^k \mu_{yx}^k}, \quad \tilde{Q}_{22}^k = \frac{E_y^k}{1-\mu_{xy}^k \mu_{yx}^k}, \\ \tilde{Q}_{12}^k &= \frac{\mu_{xy}^k E_x^k}{1-\mu_{xy}^k \mu_{yx}^k} = \frac{\mu_{yx}^k E_y^k}{1-\mu_{xy}^k \mu_{yx}^k}, \\ \tilde{Q}_{66}^k &= G_{xy}^k, \end{aligned} \quad (7)$$

where $E_x^k$, $E_y^k$ and $E_z^k$ are Young's modulus in the principal material directions of the $k$th layer, respectively; correspondingly, $\mu_{xy}^k$ and $\mu_{yx}^k$ are the Poisson's ratios, and $G_{xy}^k$ is the shear modulus.

### 2.2. Transformation of stiffness matrix

The stiffness matrices given in Eqs. (5)–(7) are based on the coordinate system aligned with the principal material directions of the $k$th layer. However, to analyze the mechanical behaviors of the whole multilayer microplate, the stiffness matrices need to be transformed into a common coordinate system. As shown in Fig. 2, $x^k$, $y^k$ and $z^k$ are the axes of the coordinate system aligned with the principal material directions of the $k$th layer, and $x$, $y$ and $z$ are the axes of the common coordinate system of the whole multilayer microplate. Assuming that the angle, $\theta^k$, between the two coordinate systems is taken positive by rotating the $xy$ plane counter-clockwise to the $x^k y^k$ plane around the $z$-axis, the stiffness matrix in the common coordinate system can be obtained by:

$$Q^k = T^{-1} \tilde{Q}^k T^{-T} = \begin{bmatrix} Q_{11}^k & Q_{12}^k & 0 \\ Q_{12}^k & Q_{22}^k & 0 \\ 0 & 0 & Q_{66}^k \end{bmatrix} \quad (8)$$

where $\boldsymbol{T}^{-1}$ and $\boldsymbol{T}^{-\mathrm{T}}$ are given in Eqs. (A.1)–(A.4) in Appendix A, and $\boldsymbol{Q}^k$ is the stiffness matrix in the common coordinate system [54]. As such, the stress–strain relationships can be rewritten as:

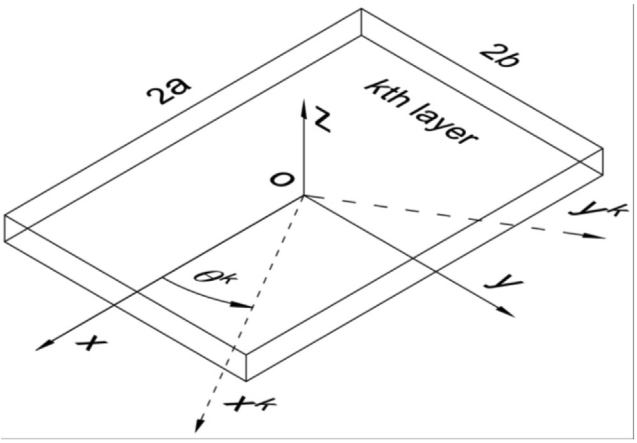


**Fig. 2.** Coordinate system for the transformation of stiffness matrix.

$$\begin{bmatrix} \sigma_x^k \\ \sigma_y^k \\ \tau_{xy}^k \end{bmatrix} = \begin{bmatrix} Q_{11}^k & Q_{12}^k & 0 \\ Q_{12}^k & Q_{22}^k & 0 \\ 0 & 0 & Q_{66}^k \end{bmatrix} \begin{bmatrix} \varepsilon_x^k \\ \varepsilon_y^k \\ \gamma_{xy}^k \end{bmatrix} \quad (9)$$

where $\sigma_x^k$ ($\varepsilon k\ x$) and $\sigma_y^k$ ($\varepsilon k\ y$) are the stresses (strains) in the $x$ and $y$ axes of the common coordinate system, respectively; $\tau_{xy}^k$ ($\gamma_{xy}^k$) is the shear stresses (shear strains) in the $xy$ plane.

### 2.3. Moments and force distribution

The bending moments of multilayer anisotropic microplates can be obtained by integrating the stresses over the $n$ layers and summing the resultant integration:

$$\begin{bmatrix} M_x \\ M_y \\ M_{xy} \end{bmatrix} = \sum_{k=1}^{n} \int_{Z_{k-1}}^{Z_k} \begin{bmatrix} \sigma_x^k \\ \sigma_y^k \\ \tau_{xy}^k \end{bmatrix} z dz \quad (10)$$

Substituting the relationships between the strain and deflection given by Eq. (11) into Eq. (9),

$$\begin{bmatrix} \varepsilon_x & \varepsilon_y & \gamma_{xy} \end{bmatrix}^{\mathrm{T}} = -z \begin{bmatrix} \frac{\partial^2 w}{\partial x^2} & \frac{\partial^2 w}{\partial y^2} & 2\frac{\partial^2 w}{\partial x \partial y} \end{bmatrix}^{\mathrm{T}} \quad (11)$$

and then substituting the resultant equation into (10), the bending moments can be rewritten as:

$$\begin{bmatrix} M_x \\ M_y \\ M_{xy} \end{bmatrix} = -\begin{bmatrix} D_{11} & D_{12} & 0 \\ D_{12} & D_{22} & 0 \\ 0 & 0 & D_{66} \end{bmatrix} \begin{bmatrix} \frac{\partial^2 w}{\partial x^2} \\ \frac{\partial^2 w}{\partial y^2} \\ 2\frac{\partial^2 w}{\partial x \partial y} \end{bmatrix} \quad (12)$$

where $D_{11}$, $D_{12}$, $D_{22}$ and $D_{66}$ are stiffnesses of the whole microplate, which can be given as:

$$\begin{aligned} D_{11} &= \frac{1}{3} \sum_{k=1}^{n} Q_{11}^k (z_k^3 - z_{k-1}^3) \\ D_{12} &= \frac{1}{3} \sum_{k=1}^{n} Q_{12}^k (z_k^3 - z_{k-1}^3) \\ D_{22} &= \frac{1}{3} \sum_{k=1}^{n} Q_{22}^k (z_k^3 - z_{k-1}^3) \\ D_{66} &= \frac{1}{3} \sum_{k=1}^{n} Q_{66}^k (z_k^3 - z_{k-1}^3) \end{aligned} \quad (13)$$

### 2.4. Residual stress

Residual stress is induced by the fabrication processes and mismatch of thermal expansion coefficients between different components of electrostatically actuated microplate-based devices. Assuming that the residual stress in each layer is biaxial stress and is constant in both $x$ and $y$ direction [55], the overall residual stress acting on the multilayer anisotropic microplate can be obtained by:

$$N_x = \sum_{k=1}^{n} \int_{Z_{k-1}}^{Z_k} \sigma_{rx}^k dz$$
$$N_y = \sum_{k=1}^{n} \int_{Z_{k-1}}^{Z_k} \sigma_{ry}^k dz \tag{14}$$

where $\sigma_{rx}^k$ and $\sigma_{ry}^k$, are the residual stress of the $k$th layer, respectively; correspondingly, $N_x$ and $N_y$ are the overall residual stresses.

### 2.5. Nonlinear partial differential equation

By taking advantage of force equilibrium, the equation governing the deflection of the rectangular multilayer anisotropic microplate under electrostatic force, residual stress and hydrostatic pressure with time, $t$, can be obtained as:

$$\frac{\partial^2 M_x}{\partial x^2} + 2\frac{\partial M_{xy}}{\partial x \partial y} + \frac{\partial^2 M_y}{\partial y^2} + \rho_e h_e \frac{\partial^2 w}{\partial t^2} = P + F_e + N_x \frac{\partial^2 w}{\partial x^2} + N_y \frac{\partial^2 w}{\partial y^2} \tag{15}$$

where $\rho_e$ and $h_e$ are the equivalent density and thickness of the whole microplate (given in Eqs. (A.5) and (A.6) in Appendix A); $P$ is hydrostatic pressure, and $F_e$ is the electrostatic force which is given by:

$$F_e = \frac{\varepsilon_0 V^2}{2(d_0 - w)^2} \tag{16}$$

and $\varepsilon_0$ is the permittivity of the vacuum; $V$ is the sum of the applied DC and AC voltages, which can be expressed as:

$$V = V_{DC} + V_{AC}(t) \tag{17}$$

Assuming that the residual stress $N_x$ and $N_y$ are equal to each other [56] and substituting Eq. (12) into Eq. (15), the deflection governing equation can be rewritten as:

$$D_x \frac{\partial^4 w}{\partial x^4} + 2D_k \frac{\partial^4 w}{\partial x^2 \partial y^2} + D_y \frac{\partial^4 w}{\partial x^4} + \rho_e h_e \frac{\partial^2 w}{\partial t^2} = P + \frac{\varepsilon_0 V^2}{2[d_0 - w]^2} + N\left(\frac{\partial^2 w}{\partial x^2} + \frac{\partial^2 w}{\partial y^2}\right) \tag{18}$$

where $D_x$, $D_k$, $D_y$ and $N$ are given as:

$$D_x = D_{11},\ D_y = D_{22},\quad D_k = D_{12} + 2D_{66},\quad N = N_x = N_y, \tag{19}$$

and $w$ can be given as:

$$w(x,y,t) = w_{DC}(x,y) + w_{AC}(x,y,t) = \sum_{i,j=0}^{M_1} b_{ij}\phi_{ij}(x,y) + \sum_{l,m=0}^{M_2} \lambda_{lm}\eta_{lm}(x,y)\sin(\omega t + \varphi) \tag{20}$$

where $w_{DC}(x, y)$ represents the static deflection under the applied DC voltage, and $w_{AC}$ $(x, y, t)$ is the vibration around the static deflection, induced by the applied AC voltages; $\phi_{ij}$ and $\eta_{ij}$ represent the trail functions for static deflection and vibrations, respectively; $b_{ij}$ and $\lambda_{ij}$ are the coefficients to be determined, and $\varphi$ is the initial phase angle.

As clamped rectangular multilayer anisotropic microplates are concerned in this study, the deflection function $w(x, y, t)$ should satisfy the following boundary conditions:

$$w(x,y,t) = 0 \text{ and } \frac{dw(x,y,t)}{dx} = 0 \text{ at } x = \pm a$$
$$w(x,y,t) = 0 \text{ and } \frac{dw(x,y,t)}{dy} = 0 \text{ at } y = \pm b \tag{21}$$

## 3. Static behavior analysis

### 3.1. Static deflection

To analyze the static deflection under DC voltage, residual stress and hydrostatic pressure, we established a reduced-order model for Eq. (18) with the time-related terms eliminated. The trail functions used to model the deformation shape of the rectangular anisotropic microplate are chosen as:

$$\phi_{ij} = \cos^2\left(\frac{(2i+1)\pi x}{2a}\right)\cos^2\left(\frac{(2j+1)\pi y}{2b}\right),\ i,\ j = 0,\ 2,\ 4\cdots \tag{22}$$

where $i$ and $j$ even numbers. Subsequently, substituting Eqs. (20) and (22) into Eq. (18), taking a partial expansion method to approximate the electrostatic force (see Eq. (B.1) for the approximation method in Appendix B) and multiply both sides with $(d_0\text{-}w_{DC})$ and $\phi_{kl}$, a reduced-order model for the static deflection analysis can be obtained as:

$$\begin{aligned}\sum_{i,j=0}^{M_1} b_{ij} \iint (D_x \tfrac{\partial^4 \phi_{ij}}{\partial x^4} + 2D_k \tfrac{\partial^4 \phi_{ij}}{\partial x^2 \partial y^2} + D_y \tfrac{\partial^4 \phi_{ij}}{\partial y^4})(d_0\phi_{kl} - \sum_{i,j=0}^{M_1} b_{ij}\phi_{ij}\phi_{kl})dxdy \\ = \tfrac{\varepsilon_0 V_{DC}^2}{2d_0}\left(\iint \phi_{kl}dxdy + \tfrac{1}{d_0}\sum_{i,j=0}^{M_1} b_{ij}\iint \phi_{ij}\phi_{kl}dxdy \right. \\ \left. + \tfrac{1}{d_0^2}\sum_{i,j,m,n=0}^{M_1} b_{ij}b_{mn}\iint \phi_{ij}\phi_{mn}\phi_{kl}dxdy + \cdots\right) \\ + P\left(d_0\iint \phi_{kl}dxdy - \sum_{i,j=0}^{M_1} b_{ij}\iint \phi_{ij}\phi_{kl}dxdy\right) \\ + N\left(d_0\iint \nabla^2 w \times \phi_{kl}dxdy - \sum_{i,j=0}^{M_1} b_{ij}\iint \nabla^2 w \times \phi_{ij}\phi_{kl}dxdy\right) \\ i,j,m,n,k,l = 0,2,4\cdots\end{aligned} \tag{23}$$

As such, a closed-form expression for the static deflection can be derived from Eq. (23) by using both first-order terms of the trail functions and electrostatic force expansions, which is obtained as:

$$w_{DC} = \frac{A + 9a^4b^4(P-Q) - \sqrt{[A + 9a^4b^4(P-Q)]^2 - 32a^4b^4\pi^2 d_0(P+Q)B}}{\pi^2 B}\cos^2\left(\frac{\pi x}{2a}\right)\cos^2\left(\frac{\pi y}{2b}\right) \tag{24}$$

where

$$Q = \frac{\varepsilon_0 V_{DC}^2}{2d_0^2} \tag{25}$$

$$A = 3\pi^2 a^2 b^2 (a^2 + b^2)d_0 N + \pi^4(3a^4 D_y + 2a^2 b^2 D_k + 3b^4 D_x)d_0 \tag{26}$$

and

$$B = 5a^2b^2(a^2 + b^2)N + \pi^2(5a^4 D_y + 4a^2 b^2 D_k + 5b^4 D_x) \tag{27}$$

### 3.2. Pull-in voltage

The pull-in phenomenon occurs when the deflection, $w_{DC}$, reaches its maximum value, which represents the critical pull-in position. Setting the third term in the numerator of Eq. (24) to be zero and evaluating the resultant equation, the pull-in voltage of electrostatically actuated rectangular multilayer anisotropic microplates under residual stress and hydrostatic pressure can be obtained as:

$$V_{pi} = \frac{d_0\sqrt{18A + 162a^4b^4P + 32\pi^2 d_0 B - 8\pi\sqrt{d_0 B(18A + 324a^4b^4P + 16\pi^2 d_0 B)}}}{9a^2b^2\sqrt{\varepsilon_0}} \tag{28}$$

## 4. Resonant frequency for small-amplitude vibrations

To analyze the resonant frequencies of the multilayer anisotropic microplate under DC and AC voltages, as well as residual stress and hydrostatic pressure, we used the same trail functions as Eq. (22) to simulate the mode shape, that is:

$$\eta_{lm}(x,y) = \cos^2\left(\frac{(2l+1)\pi x}{2a}\right)\cos^2\left(\frac{(2m+1)\pi y}{2b}\right),\ l,\ m = 0,\ 2,\ 4\cdots \tag{29}$$

For small-amplitude vibrations, the applied DC voltage is much larger than the AC voltage [5,21,24,31,33,35]. Therefore, substituting Eqs. (29) and (20) into Eq. (18) and eliminating the time-independent terms in the resultant equation, then expanding the electrostatic force at ($w_{DC}$, $V_{DC}$) and eliminating those higher-order terms, a simplified equation determining the resonant frequency is obtained as:

$$D_x\frac{\partial^4 w_{AC}}{\partial x^4}+2D_k\frac{\partial^4 w_{AC}}{\partial x^2\partial y^2}+D_y\frac{\partial^4 w_{AC}}{\partial x^4}+\rho_e h_e\frac{\partial^2 w_{AC}}{\partial t^2}=\frac{\varepsilon_0 V_{DC}^2}{(d_0-w_{DC})^3}w_{AC}+N\left(\frac{\partial^2 w_{AC}}{\partial x^2}+\frac{\partial^2 w_{AC}}{\partial y^2}\right) \tag{30}$$

To obtain a closed-form solution, a reduced-order model is established by using the same method as that for Eq. (23), but where the $V_{DC}$-included term in Eq. (30) is approximated by Eq. (B.2) in Appendix B. As such, the model for the small-amplitude vibration can be obtained as:

$$\begin{aligned}&\sum_{l,m=0}^{M_2}\lambda_{lm}\iint\left(\left(D_x\frac{\partial^4\eta_{lm}}{\partial x^4}+2D_k\frac{\partial^4\eta_{lm}}{\partial x^2\partial y^2}+D_y\frac{\partial^4\eta_{lm}}{\partial y^4}\right)-\omega^2\rho_e h_e\eta_{lm}\right)(d_0-w_{DC}^2)^2\eta_{ij}\mathrm{d}x\mathrm{d}y\times\sin(\omega t+\varphi)\\&=\frac{\varepsilon_0 V_{DC}^2}{d_0}\left(\sum_{l,m=0}^{M_2}\lambda_{lm}\iint\eta_{lm}\eta_{ij}\mathrm{d}x\mathrm{d}y+\frac{1}{d_0}\sum_{l,m=0}^{M_2}\lambda_{lm}\iint w_{DC}\eta_{lm}\eta_{ij}\mathrm{d}x\mathrm{d}y\right.\\&\left.+\frac{1}{d_0^2}\sum_{l,m=0}^{M_2}\lambda_{lm}\iint w_{DC}^2\eta_{lm}\eta_{ij}\mathrm{d}x\mathrm{d}y+\cdots\right)\sin(\omega t+\varphi)+N\iint\nabla^2 w_{AC}\times(d_0-w_{DC}^2)^2\eta_{ij}\mathrm{d}x\mathrm{d}y\\&l,m,i,j=0,2,4\cdots\end{aligned} \tag{31}$$

where

$$\nabla^2 w_{AC}=\frac{\partial^2 w_{AC}}{\partial x^2}+\frac{\partial^2 w_{AC}}{\partial y^2} \tag{32}$$

Subsequently, a solution to the angular frequency can be derived from Eq. (31) by using both first-order terms of the expanded electrostatic force and trail functions, as being:

$$\begin{aligned}\omega=\frac{1}{ra^2}\{&[r^2\pi^4 HD_x+2\pi^4(225C^2-512Cd_0+256d_0^2)D_k+r^{-2}\pi^4 HD_y\\&+(1+r^2)\pi^2a^2HN-128r^2a^4(25C+36d_0)Q]/\\&\left[(1225C^2-3200Cd_0+2304d_0^2)h_e\rho_e\right]\}^{1/2}\end{aligned} \tag{33}$$

where $r = b/a$,

$$H=525C^2-1280Cd_0+768d_0^2 \tag{34}$$

and

$$C=\{A-[A^2-32\pi^2r^4a^8d_0(P+Q)B]^{1/2}\}/(\pi^2B) \tag{35}$$

Finally, a closed-form expression for the resonant frequency of electrostatically actuated multilayered anisotropic microplates under residual stress and hydrostatic pressure can be rewritten as:

$$\begin{aligned}f=\frac{1}{2\pi ra^2}\{&[r^2\pi^4 HD_x+2\pi^4(225C^2-512Cd_0+256d_0^2)D_k+r^{-2}\pi^4 HD_y\\&+(1+r^2)\pi^2a^2HN-128r^2a^4(25C+36d_0)Q]/[(1225C^2-3200Cd_0\\&+2304d_0^2)h_e\rho_e]\}^{1/2}\end{aligned} \tag{36}$$

Eqs. (24), (28) and (36) can also be applied to the analysis of the corresponding mechanical behavior analyses of electrostatically actuated multilayer microplates with isotropic material properties where $D_x$, $D_y$ and $D_k$ are equal to each other.

## 5. Analysis accuracy and generality evaluation of closed-form expressions

### 5.1. Accuracy and generality study using FEM simulations

To analyze the accuracy and generality of our closed-form expressions, we established a 3D electromechanical coupling model for a square anisotropic microplate using ANSYS 15.0. SOLID185 and TRANS126 elements were used to model the microplate and electromechanical coupling field between the top and bottom electrodes, respectively. The material of the plate was assumed to be (1 0 0) silicon, and the coordinate system of the plate was aligned with the principal material directions of the silicon, [1 1 0] directions, to directly use its elastic constants as shown in Table 1. The meshing number was optimized to obtain reliable numerical results (about 0.05% relative difference between the results of two different meshings with 100 element difference). Static and pre-stressed modal analyses were performed to obtain numerical solutions to the deflections, pull-in voltages and resonant frequencies under different electrostatic forces, residual stresses and hydrostatic pressures. The dimensions of the studied electrostatically actuated microplate were 60 μm in width, 1 μm in thickness and 0.6 μm in gap distance.

To demonstrate the necessity of taking the material anisotropy into account in the analysis of the mechanical behaviors of electrostatically actuated anisotropic microplates, we compared the deflection, resonant frequency and pull-in voltage calculated using anisotropic elastic constants with those calculated using the isotropic ones frequently used in previous analyses [52]. We observed that the theoretical results using anisotropic elastic constants almost overlapped with those from the FEM simulations (Fig. 3a-i and b-i), showing the maximum relative differences of 3.4% and 4.5% for the static deflection and resonant frequency at the DC voltages up to 96% of the pull-in voltages (Fig. 3a-ii and b-ii), respectively. However, the theoretical deflections (resonant frequencies) based on the isotropic elastic constants show the maximum difference of over 47% (73%) from the FEM simulation results, which is 10 (15) times larger than that of those based on the anisotropic elastic constants (Fig. 3a-ii and b-ii). Additionally, a comparison of the pull-in voltage indicates our closed-form expressions could contribute to at least 5 times improvement in the analysis accuracy compared with that without consideration of the material anisotropy (Table 2). These results demonstrate that considering material anisotropy in theoretical analysis can significantly improve the analysis accuracy of these mechanical parameters of electrostatically actuated anisotropic microplates.

Subsequently, to evaluate their accuracy and applicability to a wide dimension range of electrostatically actuated anisotropic microplates, we conducted a parametric study on the derived closed-form expressions by changing one dimension and keeping the others fixed. We first changed the length of the square anisotropic microplate from 20 μm to 100 μm. The resultant pull-in voltages showed a maximum relative difference of 1.65% from the numerical results within the length-to-thickness ratios of 20 to 100 (Fig. 4a). The static defections and resonant frequencies showed maximum relative differences of 4.5% and 5.8% at the DC voltages up to 96% of the pull-in voltages within the length-to-thickness ratios of 20 to 80 (Tables 3 and 4). The maximum relative differences for the static defection and resonant frequency increased to 8.8% and 11% at the length-to-thickness ratio of 100. This could be the limit of the applicable dimension range of the closed-form expressions because, above that, the microplate behaves actually like a membrane, and the middle-plane stretching effect dominates the mechanical behaviors.

Further, we compared the pull-in voltages, static deflection and resonant frequencies of the anisotropic microplate under different gap distance-to-thickness ratios. The pull-in voltages showed a maximum relative difference of 1.67% within the gap-to-thickness ratio range less than 2 (Fig. 4b). The static defections and resonant frequencies showed maximum relative differences of 3.8% and 4.5%, respectively, at the DC voltages up to 96% of pull-in voltages within the same dimension range (Table 5 and 6). These results demonstrate that the closed-form expressions have high accuracy in the mechanical behavior analyses of electrostatically actuated anisotropic microplates within a wide dimension range.

**Table 1**
The elastic constants of (1 0 0) silicon with inclusion and exclusion of its material anisotropy [45,52].

| | Young's Modulus (GPa) | Shear Modulus (GPa) | Passion's ratio | Density (kg/m$^3$) |
|---|---|---|---|---|
| Isotropic [1 0 0] | 130 ($E$) | $E$/[2(1 + $\nu$)] | 0.28 ($\nu$) | 2332 |
| Isotropic [1 1 0] | 169 ($E$) | $E$/[2(1 + $\nu$)] | 0.064 ($\nu$) | 2332 |
| Anisotropic | 169 ($E_x$) | 50.9 ($G_{xy}$) | 0.064 ($\nu_{xy}$) | 2332 |
| | 169 ($E_y$) | 79.6 ($G_{yz}$) | 0.36 ($\nu_{yz}$) | |
| | 130 ($E_z$) | 79.6 ($G_{zx}$) | 0.28 ($\nu_{zx}$) | |

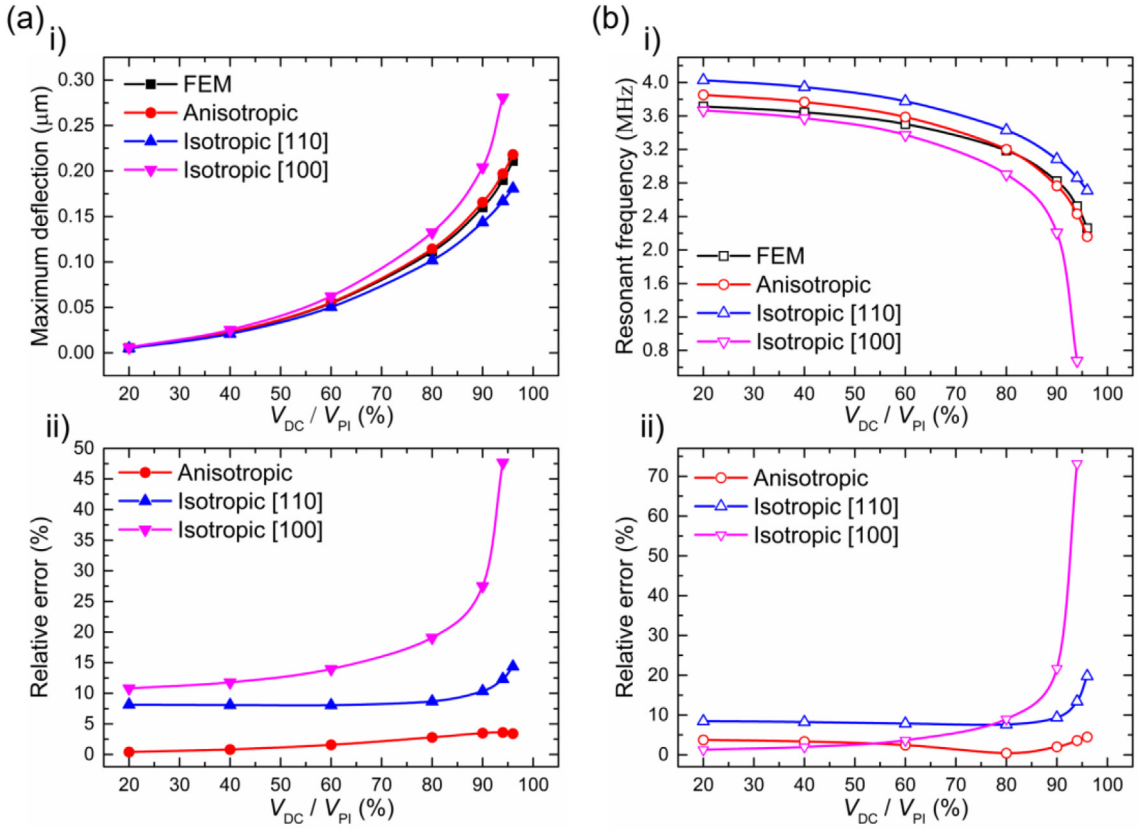


**Fig. 3.** Comparisons of the static deflections and resonant frequencies of the electrostatically actuated microplate between using anisotropic elastic constants and using isotropic elastic constants in [1 1 0] and [1 0 0] directions. (a) Static deflection comparison, where the numerical results from FEM simulations were used as a reference for error analysis; i) the static deflections under different voltages; ii) the relative error between the theoretical analysis and FEM simulations. (b) Resonant frequency comparison and error analysis; i) the resonant frequencies under different voltages; ii) relative error analysis.

**Table 2**
Pull-in voltages of the electrostatically actuated anisotropic microplate with/without the material anisotropy considered.

| Source | Anisotropic (FEM) | Anisotropic (analytical) | Isotropic [1 1 0] (analytical) | Isotropic [1 0 0] (analytical) |
|---|---|---|---|---|
| Pull-in voltage (V) | 92.4 | 91.8 | 95.4 | 87.0 |
| Rel. error | – | 0.6% | 3.2% | 5.8% |

We further evaluated the ability of our closed-form expressions to predict the mechanical behaviors of the electrostatically actuated anisotropic microplate under different residual stresses and hydrostatic pressures by changing one load and keeping the others fixed (i.e. fixing the DC voltage and pressure or fixing the DC voltage and residual stress). The comparisons showed that both analytical results under different residual stresses and different pressures had excellent consistence with the numerical ones. For example, within the studied residual stress range of −120 MPa to 120 MPa, the corresponding analytical and numerical solutions to pull-in voltages overlapped with each other, showing a maximum relative difference of 1.7% (Fig. 5a). The theoretical deflections and resonant frequencies agreed well with those numerical ones, showing the maximum difference of 4.0% and 4.3%, respectively (Fig. 5b and 5c). Furthermore, the theoretical results of static deflections, resonant frequencies and pull-in voltages under different pressures (i.e. 0 to 120 kPa) also agreed well with the numerical results (Table 7). These results demonstrate that our closed-form expressions have high accuracy in the analysis of the mechanical parameters of electrostatically actuated anisotropic microplates under different residual stresses and hydrostatic pressures.

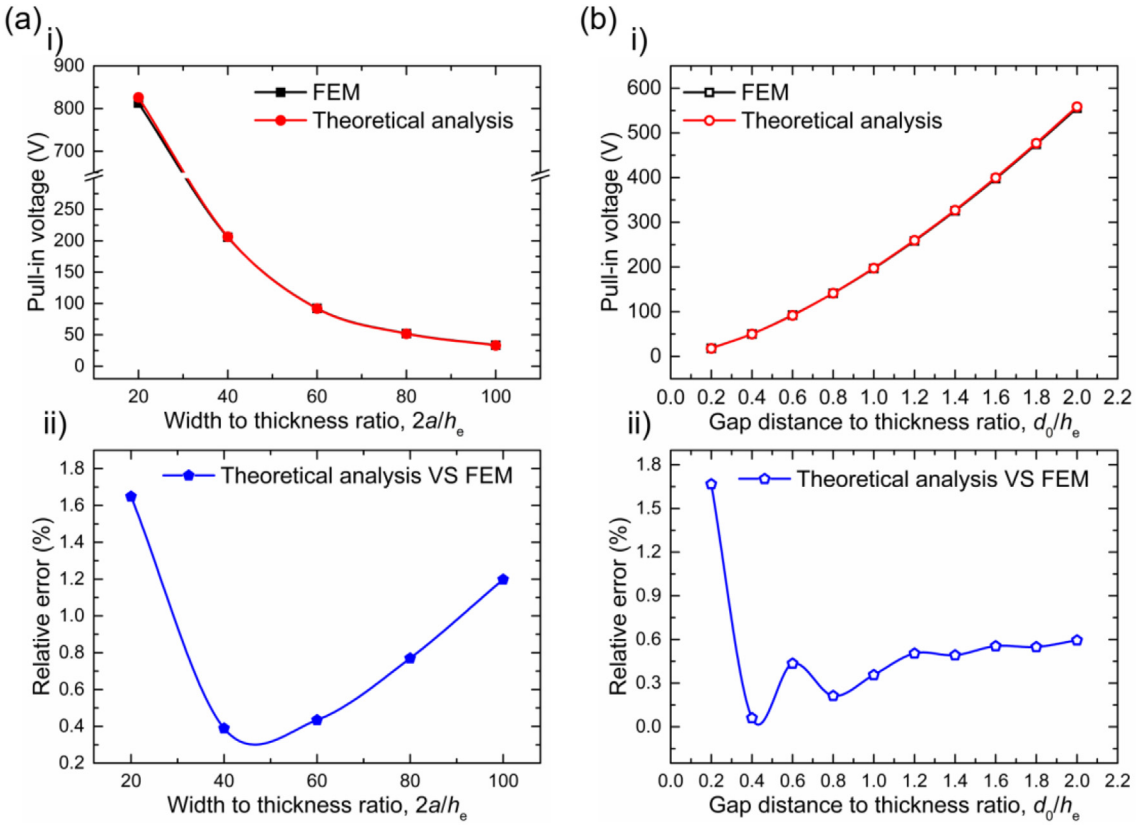


**Fig. 4.** Comparisons of pull-in voltages under different dimension ranges (a) Comparison of pull-in voltages under different width-to-thickness ratios, $2a/h_e$; i) Pull-in voltages obtained using Eq. (28) and FEM simulations; ii) Relative error between theoretical analysis and FEM simulations. (b) Comparison of pull-in voltages with different gap distance-to-thickness ratios, $d_0/h_e$; i) Pull-in voltages; ii) relative error analysis.

**Table 3**
Comparison of the maximum displacements under different length-to-thickness ratios, $2a/h_e$, (μm).

| $2a/h_e$ | Source | $V_{DC}/V_{PI}$ | | | | | | |
|---|---|---|---|---|---|---|---|---|
| | | 0.2 | 0.4 | 0.6 | 0.8 | 0.9 | 0.94 | 0.96 |
| 20 | FEM | 0.0053 | 0.0220 | 0.0531 | 0.1077 | 0.1537 | 0.1809 | 0.1988 |
| | Analytical | 0.0052 | 0.0217 | 0.0526 | 0.1073 | 0.1529 | 0.1790 | 0.1953 |
| 40 | FEM | 0.0054 | 0.0222 | 0.0536 | 0.1087 | 0.1554 | 0.1833 | 0.2019 |
| | Analytical | 0.0054 | 0.0223 | 0.0542 | 0.1111 | 0.1597 | 0.1884 | 0.2071 |
| 60 | FEM | 0.0054 | 0.0226 | 0.0546 | 0.1112 | 0.1601 | 0.1901 | 0.2109 |
| | Analytical | 0.0055 | 0.0228 | 0.0555 | 0.1143 | 0.1656 | 0.1969 | 0.2181 |
| 80 | FEM | 0.0054 | 0.0225 | 0.0545 | 0.1109 | 0.1593 | 0.1889 | 0.2092 |
| | Analytical | 0.0055 | 0.0228 | 0.0555 | 0.1145 | 0.1659 | 0.1973 | 0.2186 |
| 100 | FEM | 0.0054 | 0.0224 | 0.0541 | 0.1098 | 0.1573 | 0.1858 | 0.2048 |
| | Analytical | 0.0055 | 0.0230 | 0.0560 | 0.1157 | 0.1681 | 0.2006 | 0.2230 |

**Table 4**
Comparison of the resonant frequencies under different length-to-thickness ratios, $2a/h_e$, (Hz).

| $2a/h$ | Source | $V_{DC}/V_{PI}$ | | | | | | |
|---|---|---|---|---|---|---|---|---|
| | | 0.2 | 0.4 | 0.6 | 0.8 | 0.9 | 0.94 | 0.96 |
| 20 | FEM | 32,940,516 | 32,353,137 | 31,138,067 | 28,510,016 | 25,560,063 | 23,318,359 | 21,539,772 |
| | Analytical | 34,679,164 | 33,942,734 | 32,433,349 | 29,267,807 | 25,955,351 | 23,674,765 | 22,050,630 |
| 40 | FEM | 8,337,044 | 8,186,079 | 7,873,469 | 7,194,804 | 6,425,442 | 5,830,961 | 5,348,865 |
| | Analytical | 8,668,316 | 8,478,881 | 8,088,062 | 7,253,835 | 6,347,542 | 5,688,726 | 5,189,721 |
| 60 | FEM | 3,713,356 | 3,644,712 | 3,501,926 | 3,187,879 | 2,820,701 | 2,521,864 | 2,261,339 |
| | Analytical | 3,852,049 | 3,765,910 | 3,587,234 | 3,200,098 | 2,765,157 | 2,431,595 | 2,160,705 |
| 80 | FEM | 2,092,350 | 2,053,742 | 1,973,486 | 1,797,312 | 1,592,383 | 1,427,389 | 1,286,361 |
| | Analytical | 2,166,763 | 2,118,258 | 2,017,617 | 1,799,401 | 1,553,827 | 1,374,442 | 1,210,971 |
| 100 | FEM | 1,348,332 | 1,323,624 | 1,272,361 | 1,160,442 | 1,032,054 | 931,341 | 848,745 |
| | Analytical | 1,386,659 | 1,355,363 | 1,290,300 | 1,148,448 | 986,744 | 859,606 | 752,558 |

**Table 5**
Comparison of the maximum displacement under gap distance-to-thickness ratios less than 2, (μm).

| $d_0/h_e$ | Method | $V_{DC}/V_{PI}$ (%) | | | | | | |
|---|---|---|---|---|---|---|---|---|
| | | 20 | 40 | 60 | 80 | 90 | 94 | 96 |
| 0.2 | FEM | 0.0018 | 0.0077 | 0.0187 | 0.0382 | 0.0552 | 0.0659 | 0.0732 |
| | Analytical | 0.0019 | 0.0078 | 0.0190 | 0.0395 | 0.0577 | 0.0695 | 0.0780 |
| 0.4 | FEM | 0.0036 | 0.0149 | 0.0359 | 0.0729 | 0.1044 | 0.1233 | 0.1359 |
| | Analytical | 0.0036 | 0.0150 | 0.0365 | 0.0750 | 0.1081 | 0.1279 | 0.1410 |
| 0.6 | FEM | 0.0054 | 0.0226 | 0.0546 | 0.1112 | 0.1601 | 0.1901 | 0.2109 |
| | Analytical | 0.0055 | 0.0228 | 0.0555 | 0.1143 | 0.1656 | 0.1969 | 0.2181 |
| 0.8 | FEM | 0.0071 | 0.0296 | 0.0714 | 0.1447 | 0.2069 | 0.2439 | 0.2685 |
| | Analytical | 0.0072 | 0.0298 | 0.0725 | 0.1487 | 0.2139 | 0.2526 | 0.2778 |
| 1.0 | FEM | 0.0089 | 0.0369 | 0.0890 | 0.1803 | 0.2569 | 0.3033 | 0.3336 |
| | Analytical | 0.0089 | 0.0372 | 0.0903 | 0.1852 | 0.2662 | 0.3140 | 0.3451 |
| 1.2 | FEM | 0.0106 | 0.0441 | 0.1065 | 0.2157 | 0.3077 | 0.3622 | 0.3981 |
| | Analytical | 0.0107 | 0.0445 | 0.1081 | 0.2215 | 0.3182 | 0.3750 | 0.4118 |
| 1.4 | FEM | 0.0124 | 0.0515 | 0.1242 | 0.2516 | 0.3590 | 0.4225 | 0.4643 |
| | Analytical | 0.0125 | 0.0519 | 0.1261 | 0.2584 | 0.3711 | 0.4374 | 0.4803 |
| 1.6 | FEM | 0.0142 | 0.0588 | 0.1418 | 0.2871 | 0.4095 | 0.4818 | 0.5293 |
| | Analytical | 0.0142 | 0.0592 | 0.1439 | 0.2948 | 0.4234 | 0.4988 | 0.5476 |
| 1.8 | FEM | 0.0159 | 0.0661 | 0.1595 | 0.3229 | 0.4606 | 0.5418 | 0.5952 |
| | Analytical | 0.0160 | 0.0666 | 0.1619 | 0.3316 | 0.4762 | 0.5610 | 0.6158 |
| 2.0 | FEM | 0.0177 | 0.0734 | 0.1770 | 0.3584 | 0.5111 | 0.6010 | 0.6601 |
| | Analytical | 0.0178 | 0.0740 | 0.1797 | 0.3681 | 0.5283 | 0.6223 | 0.6829 |

**Table 6**
Comparison of the resonant frequencies under gap distance-to-thickness ratios less than 2 (Hz).

| $d_0/h_e$ | Method | $V_{DC}/V_{PI}$ (%) | | | | | | |
|---|---|---|---|---|---|---|---|---|
| | | 20 | 40 | 60 | 80 | 90 | 94 | 96 |
| 0.2 | FEM | 3,712,823 | 3,642,248 | 3,494,502 | 3,163,829 | 2,762,940 | 2,420,095 | 2,107,874 |
| | Analytical | 3,851,391 | 3,762,856 | 3,577,972 | 3,169,694 | 2,689,669 | 2,290,222 | 1,920,881 |
| 0.4 | FEM | 3,713,598 | 3,645,835 | 3,505,352 | 3,199,338 | 2,849,838 | 2,577,016 | 2,353,636 |
| | Analytical | 3,852,362 | 3,767,361 | 3,591,604 | 3,214,123 | 2,798,413 | 2,489,776 | 2,249,780 |
| 0.6 | FEM | 3,713,356 | 3,644,712 | 3,501,926 | 3,187,879 | 2,820,701 | 2,521,864 | 2,261,339 |
| | Analytical | 3,852,049 | 3,765,910 | 3,587,234 | 3,200,098 | 2,765,157 | 2,431,595 | 2,160,705 |
| 0.8 | FEM | 3,713,740 | 3,646,484 | 3,507,262 | 3,205,277 | 2,863,565 | 2,600,330 | 2,387,779 |
| | Analytical | 3,852,519 | 3,768,087 | 3,593,780 | 3,221,036 | 2,814,476 | 2,517,126 | 2,290,222 |
| 1.0 | FEM | 3,713,802 | 3,646,770 | 3,508,101 | 3,207,888 | 2,872,723 | 2,610,947 | 2,403,888 |
| | Analytical | 3,852,586 | 3,768,398 | 3,594,712 | 3,223,984 | 2,821,261 | 2,528,543 | 2,306,862 |
| 1.2 | FEM | 3,713,860 | 3,647,030 | 3,508,864 | 3,210,251 | 2,875,170 | 2,620,450 | 2,418,229 |
| | Analytical | 3,852,647 | 3,768,678 | 3,595,551 | 3,226,626 | 2,827,312 | 2,538,658 | 2,321,492 |
| 1.4 | FEM | 3,713,871 | 3,647,081 | 3,508,994 | 3,210,568 | 2,875,754 | 2,621,312 | 2,419,376 |
| | Analytical | 3,852,650 | 3,768,694 | 3,595,598 | 3,226,774 | 2,827,649 | 2,539,220 | 2,322,303 |
| 1.6 | FEM | 3,713,902 | 3,647,218 | 3,509,386 | 3,211,731 | 2,878,365 | 2,625,729 | 2,425,939 |
| | Analytical | 3,852,677 | 3,768,819 | 3,595,972 | 3,227,952 | 2,830,336 | 2,543,690 | 2,328,733 |
| 1.8 | FEM | 3,713,914 | 3,647,269 | 3,509,519 | 3,212,058 | 2,878,976 | 2,626,647 | 2,427,188 |
| | Analytical | 3,852,681 | 3,768,836 | 3,596,022 | 3,228,110 | 2,830,697 | 2,544,290 | 2,329,595 |
| 2.0 | FEM | 3,713,940 | 3,647,384 | 3,509,843 | 3,213,001 | 2,881,058 | 2,630,133 | 2,432,328 |
| | Analytical | 3,852,702 | 3,768,932 | 3,596,312 | 3,229,020 | 2,832,768 | 2,547,727 | 2,334,522 |

### *5.2. Experimental validation of closed-form expressions*

In the last section, we evaluated the analysis accuracy and the generality of our closed-form expressions using FEM simulations. Herein, CMUTs with a three-layer vibrating microplate were fabricated to experimentally verify the theoretical expressions. As shown in Fig. 6 (a) and (b), the vibrating microplate consists of the (1 0 0) silicon, $SiO_2$ and aluminum layers with a gap distance of $d_0$, which has an initial deflection of 0.113 μm caused by the co-action of residual stress and atmospheric pressure (see Table C1 for the tested structure parameters in Appendix C). Fig. 6 (c) and (d) show the comparisons of the static deflections and resonant frequencies of the CMUTs between experimental and theoretical results, under different DC voltages and a fixed pressure of 0.1 MPa and initial residual stress of 140 Mpa (see Appendix C for the testing method for the experimental data and calculation of the theoretical results). Both experimental results of the defection and resonant frequency show good consistence with their theoretical results, with the maximum differences of 6.3% in the resonant frequency analysis. Furthermore, the theoretical pull-in voltage (53 V) agreed well with the measured pull-in voltage (more than 47 V). The differences of the theoretical results from the experimental ones are larger than those from the FEM simulations demonstrated in previous sections. The increased difference could be caused by the electrode charging problem in CMUTs, which can cause an external positive or negative voltage superimposed on the applied DC voltages and result in a larger difference in deflection and resonant frequency than the expected value [57]. The difference can be further reduced by eliminating the electrode charging problem or by estimating the caused external voltages. Taken together, the above results experimentally validated the capability of our closed-form expressions in the mechanical parameter analysis of electrostatically actuated multilayer anisotropic microplates.

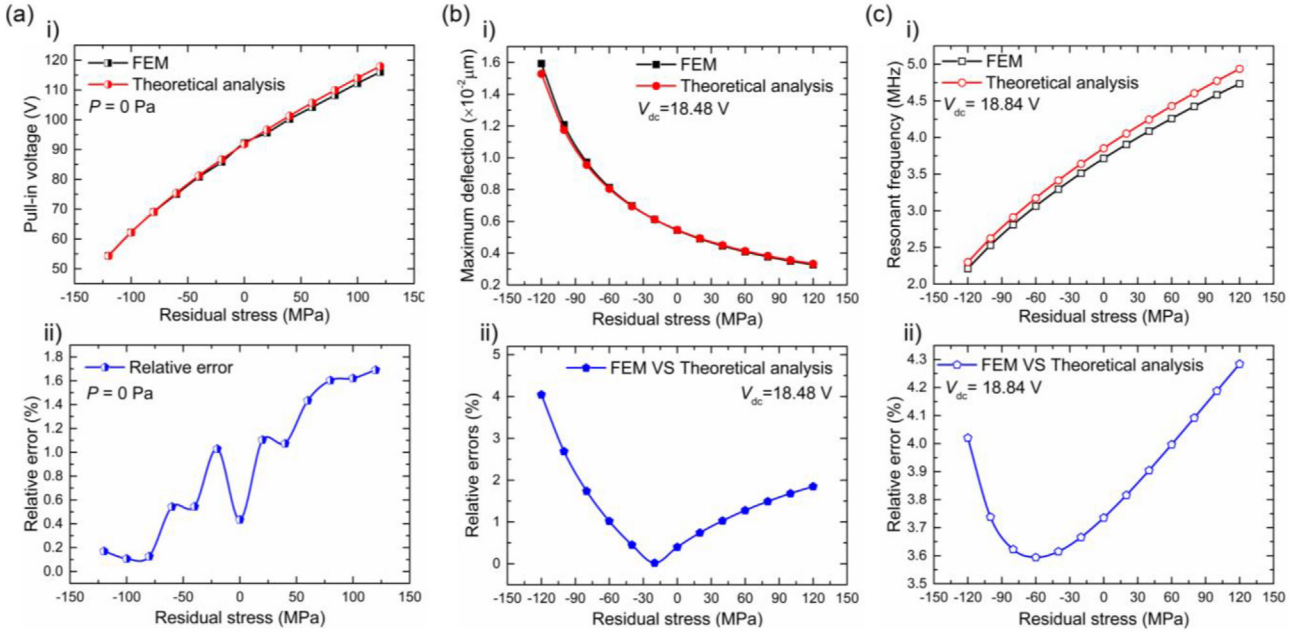


**Fig. 5.** Comparison of the pull-in voltages, deflections and resonant frequencies of the electrostatically actuated microplates between analytical and numerical results under different residual stresses, where the basic dimensions mentioned before were used. (a) Pull-in voltage comparison under different residual stresses at a fixed pressure of 0 Pa; i) the analytical and numerical solutions to pull-in voltages; ii) the relative error analysis. (b) Static deflection comparison; i) the analytical and numerical solutions to deflections under different residual stress with a fixed DC voltage of 18.84 V and a fixed pressure of 0 Pa; ii) the relative error analysis. (c) Resonant frequency comparison; i) the analytical and numerical solutions to resonant frequencies under different residual stresses, but the same voltage and pressure as the deflection analysis; ii) relative error analysis.

**Table 7**
Comparisons of the maximum deflections, resonant frequencies and pull-in voltages under different pressures with a fixed $V_{DC}$ of 20% $V_{PI}$.

| Mechanical variable | Method | Pressure (kPa) | | | | | |
|---|---|---|---|---|---|---|---|
| | | 0 | 20 | 40 | 60 | 80 | 100 |
| Deflection (μm) | FEM | 0.00544 | 0.0314 | 0.0574 | 0.0834 | 0.110 | 0.136 |
| | Analytical | 0.00546 | 0.0319 | 0.0592 | 0.0876 | 0.117 | 0.148 |
| Resonant frequency (Hz) | FEM | 3,713,356 | 3,711,290 | 3,708,889 | 3,706,081 | 3,702,773 | 3,698,840 |
| | Analytical | 3,698,840 | 3,819,257 | 3,782,297 | 3,740,161 | 3,691,437 | 3,634,045 |
| Pull-in voltage (V) | FEM | 92.4 | 88.0 | 82.8 | 78.0 | 73.4 | 64.7 |
| | Analytical | 91.8 | 86.8 | 81.6 | 76.3 | 70.7 | 68.0 |

## 6. Discussion

### 6.1. Electrostatic softening effects

The parametric study in Section 5.1 shows that the closed-form expression based on the CLTP theory has high accuracy in the analysis of the deflection of electrostatically actuated microplates, even when the deflection increases up to its thickness. However, for microplates under common forces such as pressure and stress, the analysis error generally becomes larger than 5% as the deflection reaches above 20% of its thickness because of the increased middle-plane stretching [58,59]. To understand this phenomenon, we further studied the stiffness variations of electrostatically actuated microplates with/without consideration of the middle-plane stretching effects. We first derived the stiffness of a square anisotropic microplate from its deflection under hydrostatic pressure (Eq. (D.1) in Appendix D) by:

$$D(x,y)=\frac{dP}{dw}=\frac{(3D_y+2D_k+3D_x)\pi^4}{16a^4\cos^2\left(\frac{\pi x}{2a}\right)cos^2\left(\frac{\pi y}{2a}\right)} \tag{37}$$

Subsequently, the stiffness including the electrostatic softening effects can be given by differentiating the resultant force acting on the microplate to its deflection as:

$$D_{\text{eff}}(x,y)=\frac{dF(x,y)}{dw}=D(x,y)-\frac{\varepsilon_0 V_{\text{DC}}^2}{[d_0-w(x,y)]^3} \tag{38}$$

where $F(x, y)$ is the resultant force of the restoring force and the applied electrostatic force, given as:

$$F(x,y)=D(x,y)w(x,y)-\frac{\varepsilon_0 V_{\text{dc}}^2}{2[d_0-w(x,y)]^2} \tag{39}$$

Setting $N = 0$, and $a = b$ in Eq. (24), and substituting the resulting equation as well as Eq. (37) into Eq. (38), the stiffness of electrostatically actuated anisotropic microplate can be derived as:

$$\begin{aligned}D_{\text{eff}}(x,y)&=\frac{(3D_y+2D_k+3D_x)\pi^4}{16a^4\cos^2\left(\frac{\pi x}{2a}\right)\cos^2\left(\frac{\pi y}{2a}\right)}-\frac{\varepsilon_0 V_{\text{DC}}^2}{\left[d_0-w_0\cos^2\left(\frac{\pi x}{2a}\right)\cos^2\left(\frac{\pi y}{2a}\right)\right]^3}\\&=D_0\left[\frac{1}{\cos^2\left(\frac{\pi x}{2a}\right)\cos^2\left(\frac{\pi y}{2a}\right)}-\frac{\varepsilon_0 V_{\text{DC}}^2}{D_0\left[d_0-w_0\cos^2\left(\frac{\pi x}{2a}\right)\cos^2\left(\frac{\pi y}{2a}\right)\right]^3}\right]\end{aligned} \tag{40}$$

where, $w_0$ is the deflection at the center point (0, 0), and $D_0$ is given as:

$$D_0=\frac{(3D_y+2D_k+3D_x)\pi^4}{16a^4} \tag{41}$$

Both Eqs. (39) and (40) show the distributed stiffness over the plate area, which varies in the form of the function defined by $\cos^2$ [$\pi x$/(2a)]$\cos^2$[$\pi y$/(2a)]. The difference is that the stiffness of the common

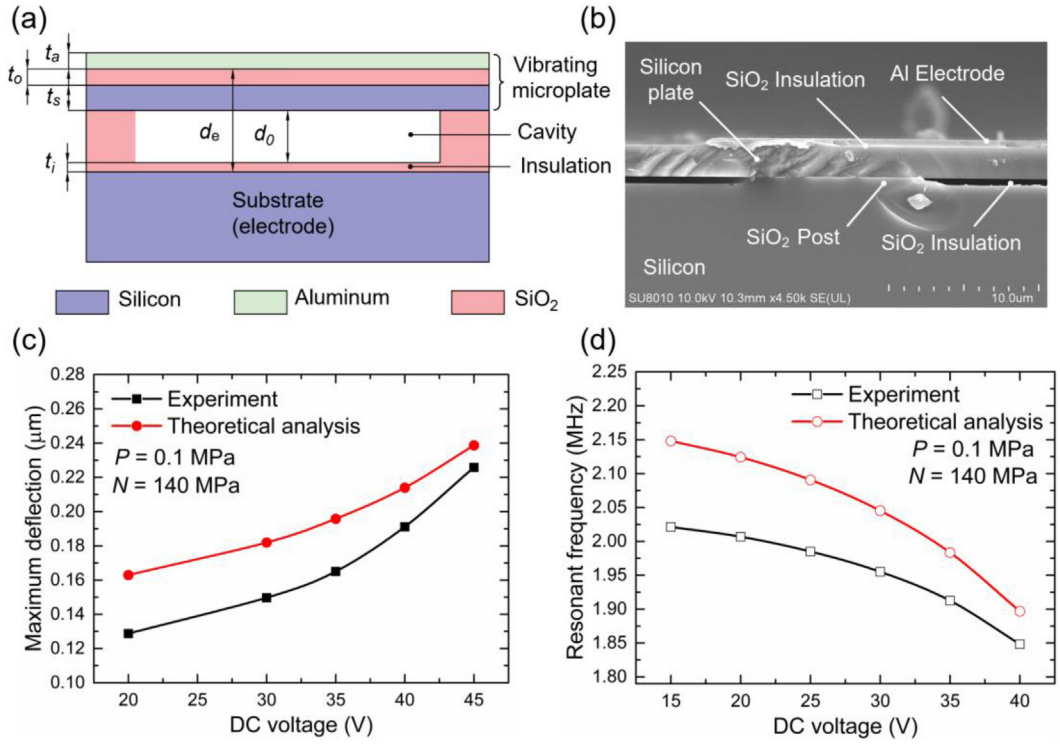


**Fig. 6.** Experimental validation of the closed-form expressions using our fabricated CMUTs with a square anisotropic microplate composed of three layers. (a) The structure schematic; (b) SEM picture of the cross-section of a CMUT cell; (c) Comparison of the static deflections under different DC voltages; (d) Comparison of the resonant frequencies under different DC voltages.

microplate remains constant during the deflection process, but the stiffness of the electrostatic microplate decreases with its deflection (electrostatic softening effects). To clearly understand this point, we further studied the stiffness at the center point by setting $x$, $y$ in Eq. (40) to be zero, thus, which can be simplified as:

$$D_{\text{eff}}(x,y) = D_0\left[1 - \frac{\varepsilon_0 V_{\text{DC}}^2}{D_0(d_0 - w_0)^3}\right] \tag{42}$$

Further, to include the effect of the middle-plane stretching [58], the effective stiffness can be rewritten as:

$$D_{\text{eff}} = D_0\left\{1 + \left[C\frac{w_0^2}{h_e^2} - \frac{\varepsilon_0 V_{\text{DC}}^2}{D_0(d_0 - w_0)^3}\right]\right\} \tag{43}$$

where the term, $Cw^2{}_0/h_e^2$, represents the effect of the middle-plane stretching on the plate stiffness (in other words, the stress-stiffening effects), and $C$ is a coefficient to be determined. Eq. (43) shows that, for electrostatically actuated microplates, the stress-stiffening effect is weakened by the electrostatic-softening effects. Further, a parametric study on the effective stiffnesses of an electrostatic microplate shows that the stiffness with only the stress-stiffening effects considered, increasing with $w_0/h_e$, is larger than that without the stress-stiffening effects considered, $D_s$; however, the stiffness with both stress-stiffening and electrostatic-softening effects considered, decreasing with $w_0/h_e$, is smaller than $D_s$, even when the deflection reaches its thickness (Fig. 7a). The softened stiffness can decrease the induced stress in the middle-plane, resulting in reduced stress-stiffening effects and thus reducing the difference between the defection analyses with and without consideration of the middle-plane stretching. This means, for electrostatic microplates, the CLTP theory can apply to a larger deflection range than that for microplates under no action of electrostatic force, without degrading the analysis accuracy. For example, the deflections from FEM simulations, where the stress-stiffening effects were turned on/off, overlapped with each other and showed a small difference of 0.7% at the deflection equal to its thickness (Fig. 7b). These results indicate that the CLTP theory can be used for the deflection analysis of electrostatic microplates in an extended range (equal to the thickness).

### 6.2. Scale effects

The study in above sections has demonstrate the applicability of the closed-form expressions across a wide range of dimension ratios (i.e. the length-to-thickness ratios), but without evaluating the applicable minimum dimension size. In fact, the intrinsic material length scale parameter has been proved to be an inevitable factor affecting the mechanical behavior of microplates when it is comparable to the plate dimension size such as the length or thickness [39,60]. Herein, the influence of the scale effects on the analysis accuracy is discussed in order to further estimate the applicable minimum dimension size of the developed closed-form expressions. For this purpose, simplified closed-form expressions (Eqs. (D.2), (D.3) and (D.4) in Appendix D) for the static deflection, pull-in voltage and resonant frequency were constructed based on isotropic microplates with the pressure and residual stress set to be zero. Taking advantage of these expressions, we compared the analytical results of the aforementioned mechanical behaviors under different material length scale parameters between using the stiffnesses neglecting ($D_s$) and considering ($D_s^l$) the scale effects, where the $D_s{}^l$ can be given based on a modified couple stress theory [61] as:

$$D_s^l = D_s\left[1 + 6(1-\nu)\frac{l^2}{h_e^2}\right] \tag{44}$$

where $l$ and $\nu$ are the length-scale parameter and Poisson's ratio of the used material of the microplate, respectively. As shown in Fig. 8a–c, the results considering the scale effects overlap with those neglecting the scale effects under a certain range of the material length-scale parame-

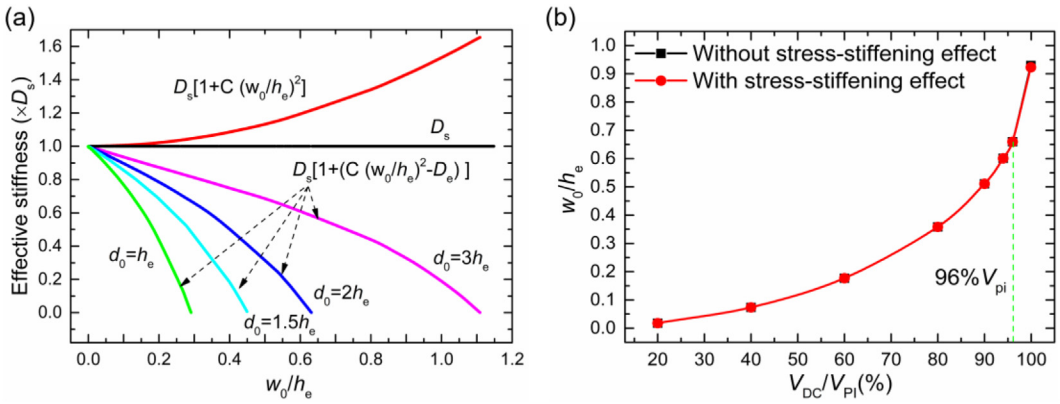


**Fig. 7.** Effective stiffness of an electrostatically actuated microplate under different conditions and comparison of the deflections with/without the inclusion of the stress-stiffening effects. (a) Effective stiffness under different deflection-to-thickness ratios, which was compared with that of the microplate without the action of electrostatic force; The effective stiffness was calculated by substituting the dimensionless deflection expression (Eq. (D.2) in Appendix D) and the stiffness $D_s$ into Eqs. (42) and (43); the coefficient $C$ for the stress-stiffening effect was derived from [58], which was 0.532; $D_s$ represents the stiffness of an isotropic microplate without the stress-stiffening effects considered, and $D_e$ represents the electrostatic softening effect, expressed by the $V_{DC}$-related term in Eq. (43); (b) The deflections of an electrostatically actuated square microplate with inclusion and exclusion of the stress-stiffness effects obtained using FEM simulations, where the basic dimensions in Section 5.1 were used.

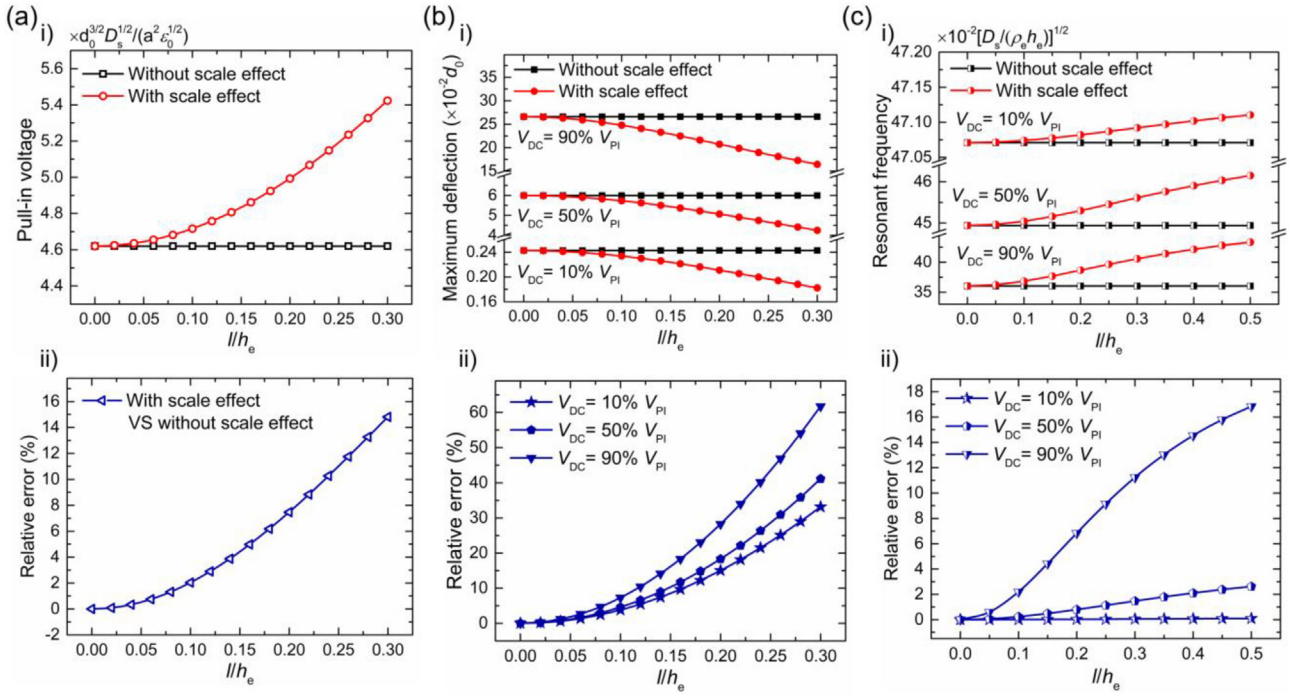


**Fig. 8.** Effects of material length-scale parameter on the analysis accuracy of the developed closed-form expressions. (a) Comparison of the pull-in voltages between neglecting and considering the scale effects. (b) Comparison of the defections beween neglecting and considering the scale effects; i) deflections under under different DC voltages; ii) relative errors. (c) Comparison of the resonant frequencies between neglecting and considering the scale effects; i) Resonant frequencies under different DC voltages; ii) relative errors. The $V_{PI}$ in (b) and (c) is the pull-in voltage without the scale effects taken into account.

ter to plate thickness ratio, $l/h_e$, while deviate significantly when the length-scale parameter increases. For the pull-in voltage, the differences between the analytical results with and without the scale effects considered is less than 5% when $l/h_e < 0.16$ (Fig. 8a-ii). The differences in the static deflection (resonant frequency) analyses are less than 7.3% when $l/h_e < 0.10$ (6.8% when $l/h_e < 0.20$) at a DC voltage of 90% $V_{PI}$, however, which decreases rapidly to 4.6% (0.8%) at a reduced DC voltage of 50% $V_{PI}$ (Fig. 8b-ii and c-ii). These results demonstrate that the influences of the scale effects on the static deflection, pull-in voltage and resonant frequency analyses are neglectable at $l/h_e <$ 0.10, 0.16 and 0.20, respectively, indicating the applicable minimum dimension sizes of the developed closed-form expressions. For electrostatic multilayer anisotropic microplates with lower dimension sizes, new modified couple stress theories considering the anisotropic elasticity can be introduced into the developed theories for accurate analysis of the scale effects [62,63].

## 7. Conclusions

In summary, we propose a general reduced-order model for electrostatically actuated rectangular microplates, which considers the material anisotropy and multilayer properties simultaneously. Closed-form

expressions for their pull-in voltage, static deflection and resonant frequency under residual stress and hydrostatic pressure are derived from this model. Analysis accuracy and general applicability of these expressions are validated using FEM simulations and experiment results of CMUTs. It is demonstrated that: 1) the closed-form expressions considering the material anisotropy can significantly improve the analysis accuracy (more than 15 times) compared with those neglecting the material anisotropy; 2) they can apply to a wide range of dimensions, i.e. within the length-to-thickness ratio of 20–100 and the distance-to-thickness ratio of ~2; 3) the closed-form expressions have high accuracy across almost the whole voltage range (i.e. from 0 to 96% of pull-in voltage), even when the deflection goes up to its thickness; 4) these expressions can also predict those mechanical parameters under different residual stresses within 4.3% difference from FEM simulations. For the effect of hydrostatic pressure, these expressions show high accuracy in a low-pressure range, which decreases with the increased pressure. For this, new methods need to be developed in the future. Additionally, the influence of electrostatic softening effects and scale effects are studied to look into the underlying reason of the high analysis accuracy and the applicable minimum dimension sizes of the developed closed-form expressions, respectively. The developed closed-form expressions in this study, more general and accurate than those based on isotropic material properties and single-layer microplates, can be widely used in the design and optimization of various MEMS sensors and actuators.

## 8. Data Availability

The raw required to reproduce these findings cannot be shared at this time due to technical or time limitations. The processed data to reproduce these findings cannot be shared at this time due to technical or time limitations.

## CRediT authorship contribution statement

**Zhikang Li:** Conceptualization, Methodology, Writing - original draft, Validation, Data curation, Investigation. **Libo Zhao:** Supervision, Visualization. **Jie Li:** Data curation, Software, Validation. **Yihe Zhao:** Data curation, Validation, Investigation. **Tingzhong Xu:** Data curation, Validation. **Zichen Liu:** Validation. **Guoxi Luo:** Writing - review & editing. **Shiming Zhang:** Writing - review & editing. **Kaiming Hu:** Conceptualization, Writing - review & editing. **Tyler Hoffman:** Writing - review & editing. **Shahid Saghir:** Conceptualization, Writing - review & editing. **Dejiang Lu:** Validation. **Wenming Zhang:** Visualization, Writing - review & editing. **Zhuangde Jiang:** Supervision.

## Declaration of Competing Interest

The authors declare that they have no known competing financial interests or personal relationships that could have appeared to influence the work reported in this paper.

## Acknowledgments

The authors would like to thank Mr. Shuaishuai Guo for his help in experiments. This work has been supported by National Natural Science Foundation of China [51805423, 51875449, 51890884, 91748207], National Science Foundation for Distinguished Young Scholars [11625208], the Research Project of State Key Laboratory of Mechanical System and Vibration [MSV201809], Natural Science Basic Research Plan in Shaanxi Province of China [2018JQ5067], the General Financial Grant from China Postdoctoral Science Foundation [2017M623160], the 111 Program [B12016], and the International Postdoctoral Exchange Fellowship Program [20180067].

## Appendix A

The matrixes $\boldsymbol{T}^{-1}$ and $\boldsymbol{T}^{\mathrm{T}}$ for the transformation of the stiffness matrix $\tilde{\boldsymbol{Q}}^{\boldsymbol{k}}$ are given as [54]:

$$T^{-1}=\begin{bmatrix}\cos^2\theta^k & \sin^2\theta^k & -2\sin\theta^k\cos\theta^k\\ \sin^2\theta^k & \cos^2\theta^k & 2\sin\theta^k\cos\theta^k\\ \sin\theta^k\cos\theta^k & -\sin\theta^k\cos\theta^k & \cos^2\theta^k-\sin^2\theta^k\end{bmatrix} \tag{A1}$$

and

$$T^{-T}=RTR^{-1} \tag{A2}$$

where the matrix $\boldsymbol{T}$ can be given as:

$$T=\begin{bmatrix}\cos^2\theta^k & \sin^2\theta^k & 2\sin\theta^k\cos\theta^k\\ \sin^2\theta^k & \cos^2\theta^k & -2\sin\theta^k\cos\theta^k\\ -\sin\theta^k\cos\theta^k & \sin\theta^k\cos\theta^k & \cos^2\theta^k-\sin^2\theta^k\end{bmatrix} \tag{A3}$$

and the matrix $\boldsymbol{R}$ is:

$$R=\begin{bmatrix}1 & 0 & 0\\ 0 & 1 & 0\\ 0 & 0 & 2\end{bmatrix} \tag{A4}$$

and $\boldsymbol{R}^{-1}$ is the inverse of the matrix $\boldsymbol{R}$.

The equivalent density and thickness of anisotropic microplates with $n$ layers shown in Fig. 1 can be calculated by:

$$\rho_e=\frac{h_1\rho_1+h_1\rho_2\cdots+h_n\rho_n}{h_1+h_2\cdots+h_n} \tag{A5}$$

$$h_e=h_1+h_2\cdots+h_n \tag{A6}$$

## Appendix B

Using the partial expansion method in [49], the electrostatic force given in Eq. (16) can be approximated as:

$$\begin{aligned}F_e(w)&=\frac{\varepsilon_0V_{\mathrm{DC}}^2}{2(d_0-w_{\mathrm{DC}})(d_0-w_{\mathrm{DC}})}\\&=\frac{\varepsilon_0V_{\mathrm{DC}}^2}{2d_0(d_0-w_{\mathrm{DC}})}\left(1+\frac{w_{\mathrm{DC}}}{d_0}+\frac{w_{\mathrm{DC}}^2}{d_0^2}+\frac{w_{\mathrm{DC}}^3}{d_0^3}+\cdots\right)\end{aligned} \tag{B1}$$

The $V_{\mathrm{DC}}$-related term on the right side of Eq. (30) can be approximated using a similar partial expansion method in [51]as:

$$\begin{aligned}\frac{\varepsilon_0V_{\mathrm{DC}}^2}{(d_0-w_{\mathrm{DC}})^3}w_{\mathrm{AC}}&=\frac{\varepsilon_0V_{\mathrm{DC}}^2}{(d_0-w_{\mathrm{DC}})^2(d_0-w_{\mathrm{DC}})}w_{\mathrm{AC}}\approx\frac{\varepsilon_0V_{\mathrm{dc}}^2}{d_0(d_0-w_{\mathrm{DC}})^2}\\&\left(1+\frac{w_{\mathrm{DC}}}{d_0}+\frac{w_{\mathrm{DC}}^2}{d_0^2}+\frac{w_{\mathrm{DC}}^3}{d_0^3}+\cdots\right)w_{\mathrm{AC}}\end{aligned} \tag{B2}$$

## Appendix C

The experimental results of the deflections, pull-in voltages and resonant frequencies of the CMUTs chips were measured using a white-light interference microscope (Talysurf CCI6000, Taylor Hobson Ltd., UK) and an impedance analyzer (E4990A, Agilent Technologies, Inc., USA). The DC voltages were applied using a SourceMeter (Keithley 2612A, Tektronix Inc., USA). The theoretical results of these mechan-

**Table C1**
Measured structure parameters of our fabricated CMUTs.

| Parameters | Value | Parameters | Value |
|---|---|---|---|
| Plate length ($2a/2b$) | 122.6 μm | Aluminum electrode ($t_a$) | 0.41 μm |
| Thickness of silicon plate ($t_s$) | 2.0 μm | Bottom insulation layer ($t_i$) | 0.10 μm |
| Top insulation layer ($t_o$) | 0.20 μm | Vacuum cavity ($d_0$) | 0.48 μm |

**Table C2**
Material properties of the $SiO_2$ and aluminum used for the mechanical behavior analysis of CMUTs.

| Source | Young's modulus (GPa) | Passion's ratio | Density (kg/m$^3$) | Relative permittivity |
|---|---|---|---|---|
| $SiO_2$ (isotropic) | 73.1 | 0.17 | 2270 | 3.8 |
| Aluminum (isotropic) | 67.7 | 0.35 | 2700 | – |

ical parameters were calculated using Eqs. (24), (28) and (36) under the pressure of 0.1 MPa and residual stress of 140 MPa. In the theoretical analysis, the atmospheric pressure and the residual stress were applied because they were considered as the main factors inducing the initial deflection of the microplate. The residual stress was determined using a 3D FEM model of the CMUTs based on the tested initial deflection (0.113 μm) with SOLID185 elements to simulate the layered vibrating microplates. Besides, the equivalent density $\rho_e$ and thickness $h_e$ of the multilayer microplate were obtained using Eqs. (A.5) and (A.6), respectively, and the effective electrode distance, $d_e$, can be calculated using Eq. (C.1). The stiffness of the multiplayer anisotropic microplate was obtained using Eq. (13) with the elastic constants shown in Table 1 and Table C2 because the principal material directions of (1 0 0) silicon are aligned with the common coordinate system of the vibrating microplate of the CMUT chips.

Herein, the $n$th layer of the multilayer microplate shown in Fig. 1 is assumed to be electrically conductive. Therefore, the effective electrode distance between the top and bottom elelctrodes can be equivalently given as:

$$d_e = d_0 + \frac{h_1}{\varepsilon_1} + \frac{h_2}{\varepsilon_2} \cdots + \frac{h_{n-1}}{\varepsilon_{n-1}} \tag{C1}$$

where $\varepsilon_k$ is the relative permittivity of the $k$th layer.

## Appendix D

For common thin plates under uniform force, $P$, the deflection can be derived from Eq. (18) with the electrostatic force and residual stress set to be zero. The defection function is assumed to be the same as that for Eq. (22). As such, the deflection expression can be given by

$$w(x,y) = \frac{16a^4b^4P}{(3a^4D_y + 2a^2b^2D_k + 3b^4D_x)\pi^4}\cos^2\left(\frac{\pi x}{2a}\right)\cos^2\left(\frac{\pi y}{2b}\right) \tag{D1}$$

The dimensionless expression for the displacement of the center point of the isotropic microplate under electrostatic force can be derived from Eq. (24) by setting the pressure and residual stress to be zero and $D_x = D_k = D_y = D_s$ as:

$$w_0(r) = d_0\left(0.5714 - 0.0704r^2 - 0.0704\sqrt{65.8243 - 66.7087r^2 + r^4}\right) \tag{D2}$$

where

$$r = \frac{V_{DC}}{V_{PI}},\ V_{PI} = \frac{4.62d_0^{3/2}D_s^{1/2}}{a^2\sqrt{\varepsilon_0}} \tag{D3}$$

and $D_s$ is the stiffness of isotropic microplates.

In a similar way, the dimensionless expression for the resonant frequency of isotropic microplates under electrostatic force can be derived from Eq. (36), as being:

$$f = \frac{0.2207}{a^2} \times \sqrt{\frac{D_s}{\rho_e h_e}}\left[\frac{48.259 + 5.333\sqrt{97.4091 - 74.7054r^2} + r^2(\sqrt{97.4091 - 74.7054r^2} - 53.2465)}{12.2383 - 2.9436r^2 + \sqrt{97.4901 - 74.7054r^2}}\right]^{1/2} \tag{D4}$$

The $D_s$ in Eqs. (D.2), (D.3) and (D.4) can be replaced with $D_s^l$ given in Eq. (44) to take into account the scale effect on the static defection, pull-in voltage and resonant frequency.

## References


[1] Liu G-X, Shi L-F, Li G-W, Cheng L-Y. Tri-adaptive method for improving the resolution of MEMS digital sensors. IEEE Trans Ind Electron 2019;66:8189–96.
[2] Knick CR, Sharar DJ, Wilson AA, Smith GL, Morris CJ, Bruck HA. High frequency, low power, electrically actuated shape memory alloy MEMS bimorph thermal actuators. J Micromech Microeng 2019;29.
[3] Joshi P, Kumar S, Jain VK, Akhtar J, Singh J. Distributed MEMS mass-sensor based on piezoelectric resonant micro-cantilevers. J Microelectromech Syst 2019;28:382–9.
[4] Moser J, Guttinger J, Eichler A, Esplandiu MJ, Liu DE, Dykman MI, et al. Ultrasensitive force detection with a nanotube mechanical resonator. Nat Nanotechnol. 2013;8:493–6.
[5] Bedon C, Bergamo E, Izzi M, Noè S. Prototyping and validation of MEMS accelerometers for structural health monitoring—the case study of the pietratagliata cable-stayed bridge. J Sens Actuator Networks 2018;7.
[6] Hu K-M, Zhang W-M, Yan H, Peng Z-K, Meng G. Nonlinear pull-in instability of suspended graphene-based sensors. EPL (Europhys Lett) 2019;125.
[7] Zhao L, Li J, Li Z, Zhang J, Zhao Y, Wang J, et al. Fabrication of capacitive micromachined ultrasonic transducers with low-temperature direct wafer-Bonding technology. Sens Actuators, A 2017;264:63–75.
[8] Ilyas S, Alfosail FK, Younis MI. On the response of MEMS resonators under generic electrostatic loadings: theoretical analysis. Nonlinear Dyn 2019.
[9] Bertarelli E, Ardito R, Ardito R, Corigliano A, Contro R. A plate model for the evaluation of pull-in instability occurrence in electrostatic micropump diaphragms. Int J Appl Mech 2011;03:1–19.
[10] Sheikhlou M, Shabani R, Rezazadeh G. Nonlinear analysis of electrostatically actuated diaphragm-type micropumps. Nonlinear Dyn 2015;83:951–61.
[11] Jasulaneca L, Kosmaca J, Meija R, Andzane J, Erts D. Review: electrostatically actuated nanobeam-based nanoelectromechanical switches – materials solutions and operational conditions. Beilstein J Nanotechnol 2018;9:271–300.
[12] Li Z, Zhao L, Jiang Z, Akhbari S, Ding J, Zhao Y, et al. Capacitive micromachined ultrasonic transducer for ultra-low pressure measurement: theoretical study. AIP Adv 2015;5.
[13] Pinto RMR, Brito P, Chu V, Conde JP. Thin-film silicon MEMS for dynamic mass sensing in vacuum and air: phase noise, Allan deviation, mass sensitivity and limits of detection. J Microelectromech Syst 2019;28:390–400.
[14] Kamada Y, Isobe A, Oshima T, Furubayashi Y, Ido T, Sekiguchi T. Capacitive MEMS accelerometer with perforated and electrically separated mass structure for low noise and low power. J Microelectromech Syst 2019;28:401–8.
[15] Farokhi H, Ghayesh MH. Electrically actuated MEMS resonators: effects of fringing field and viscoelasticity. Mech Syst Sig Process 2017;95:345–62.
[16] Eom K, Park HS, Yoon DS, Kwon T. Nanomechanical resonators and their applications in biological/chemical detection: Nanomechanics principles. Phys Rep 2011;503:115–63.
[17] Ilyas S, Chappanda KN, Younis MI. Exploiting nonlinearities of micro-machined resonators for filtering applications. Appl Phys Lett 2017;110.
[18] Batra RC, Porfiri M, Spinello D. Review of modeling electrostatically actuated microelectromechanical systems. Smart Mater Struct 2007;16:R23–31.
[19] Sedighi HM, Daneshmand F, Abadyan M. Dynamic instability analysis of electrostatic functionally graded doubly-clamped nano-actuators. Compos Struct 2015;124:55–64.
[20] Choi WY, Kwak YS, Park KK. Fingerprint imaging system based on capacitive micromachined ultrasonic transducer by using impediography method including direct touch and waveguide methods. IEEE Trans Ultrason Ferroelectr Freq Control. 2019;66:402–11.
[21] Qiao Y, Xu W, Sun J, Zhang H. Reliability of electrostatically actuated MEMS resonators to random mass disturbance. Mech Syst Sig Process 2019;121:711–24.
[22] Saghir S, Younis MI. An investigation of the mechanical behavior of initially curved microplates under electrostatic actuation. Acta Mech 2018;229:2909–22.
[23] Mohammadi-Alasti B, Rezazadeh G, Borgheei A-M, Minaei S, Habibifar R. On the mechanical behavior of a functionally graded micro-beam subjected to a thermal moment and nonlinear electrostatic pressure. Compos Struct 2011;93:1516–25.
[24] Zhao X, Abdel-Rahman EM, Nayfeh AH. A reduced-order model for electrically actuated microplates. J Micromech Microeng 2004;14:900–6.
[25] Saeedivahdat A, Abdolkarimzadeh F, Feyzi A, Rezazadeh G, Tarverdilo S. Effect of thermal stresses on stability and frequency response of a capacitive microphone. Microelectron J 2010;41:865–73.
[26] Talebian S, Rezazadeh G, Fathalilou M, Toosi B. Effect of temperature on pull-in voltage and natural frequency of an electrostatically actuated microplate. Mechatronics 2010;20:666–73.
[27] Nabian A, Rezazadeh G, Haddad-derafshi M, Tahmasebi A. Mechanical behavior of a circular micro plate subjected to uniform hydrostatic and non-uniform electrostatic pressure. Microsyst Technol 2007;14:235–40.

[28] Chao PCP, Chiu CW, Tsai CY. A novel method to predict the pull-in voltage in a closed form for micro-plates actuated by a distributed electrostatic force. J Micromech Microeng 2006;16:986–98.
[29] Caruntu DI, Oyervides R. Frequency response reduced order model of primary resonance of electrostatically actuated MEMS circular plate resonators. Commun Nonlinear Sci Numer Simul 2017;43:261–70.
[30] Liao L-D, Chao PCP, Huang C-W, Chiu C-W. dc dynamic and static pull-in predictions and analysis for electrostatically actuated clamped circular micro-plates based on a continuous model. J Micromech Microeng 2010;20.
[31] Vogl GW, Nayfeh AH. A reduced-order model for electrically actuated clamped circular plates. J Micromech Microeng 2005;15:684–90.
[32] Sajadi B, Alijani F, Goosen H, van Keulen F. Effect of pressure on nonlinear dynamics and instability of electrically actuated circular micro-plates. Nonlinear Dyn 2017;91:2157–70.
[33] Sajadi B, Goosen H, van Keulen F. Electrostatic instability of micro-plates subjected to differential pressure: a semi-analytical approach. Int J Mech Sci 2018;138–139:210–8.
[34] Saghir S, Younis MI. An investigation of the static and dynamic behavior of electrically actuated rectangular microplates. Int J Non Linear Mech 2016;85:81–93.
[35] Batra RC, Porfiri M, Spinello D. Reduced-order models for microelectromechanical rectangular and circular plates incorporating the Casimir force. Int J Solids Struct 2008;45:3558–83.
[36] Saghir S, Bellaredj ML, Ramini A, Younis MI. Initially curved microplates under electrostatic actuation: theory and experiment. J Micromech Microeng 2016;26.
[37] Medina L, Gilat R, Krylov S. Bistability criterion for electrostatically actuated initially curved micro plates. Int J Eng Sci 2018;130:75–92.
[38] Farokhi H, Ghayesh MH. Nonlinear mechanics of electrically actuated microplates. Int J Eng Sci 2018;123:197–213.
[39] Tahani M, Askari AR, Mohandes Y, Hassani B. Size-dependent free vibration analysis of electrostatically pre-deformed rectangular micro-plates based on the modified couple stress theory. Int J Mech Sci 2015;94–95:185–98.
[40] Ghayesh MH, Farokhi H, Amabili M. Nonlinear behaviour of electrically actuated MEMS resonators. Int J Eng Sci 2013;71:137–55.
[41] Mohammadi V, Ansari R, Faghih Shojaei M, Gholami R, Sahmani S. Size-dependent dynamic pull-in instability of hydrostatically and electrostatically actuated circular microplates. Nonlinear Dyn 2013;73:1515–26.
[42] Moghimi Zand M, Ahmadian MT. Vibrational analysis of electrostatically actuated microstructures considering nonlinear effects. Commun Nonlinear Sci Numer Simul 2009;14:1664–78.
[43] Wang Y-G, Lin W-H, Li X-M, Feng Z-J. Bending and vibration of an electrostatically actuated circular microplate in presence of Casimir force. Appl Math Model 2011;35:2348–57.
[44] Batra RC, Porfiri M, Spinello D. Vibrations and pull-in instabilities of microelectromechanical von Kármán elliptic plates incorporating the Casimir force. J Sound Vib 2008;315:939–60.
[45] Hopcroft MA, Nix WD, Kenny TW. What is the Young's Modulus of Silicon?. J Microelectromech Syst 2010;19:229–38.
[46] Thomsen EV, Reck K, Skands G, Bertelsen C, Hansen OJS, Physical AA. Silicon as an anisotropic mechanical material: Deflection of thin crystalline plates. 2014;220:347–64.
[47] Zhang Y, Zhao Y-p. Numerical and analytical study on the pull-in instability of micro-structure under electrostatic loading. Sens Actuators, A 2006;127:366–80.
[48] Porfiri M. Vibrations of parallel arrays of electrostatically actuated microplates. J Sound Vib 2008;315:1071–85.
[49] Li Z, Zhao L, Jiang Z, Ye Z, Zhao Y. An improved method for the mechanical behavior analysis of electrostatically actuated microplates under uniform hydrostatic pressure. J Microelectromech Syst 2015;24:474–85.
[50] Li Z, Zhao L, Jiang Z, Ye Z, Dai L, Zhao Y. Mechanical behavior analysis on electrostatically actuated rectangular microplates. J Micromech Microeng 2015;25.
[51] Li Z, Zhao L, Jiang Z, Zhao Y, Li J, Zhang J, et al. A closed-form approach for the resonant frequency analysis of clamped rectangular microplates under distributed electrostatic force. Sens Actuators, A 2018;280:447–58.
[52] la Cour MF, Christiansen TL, Jensen JA, Thomsen EV. Electrostatic and small-signal analysis of CMUTs with circular and square anisotropic plates. IEEE Trans Ultrason Ferroelectr Freq Control 2015;62:1563–79.
[53] Aydogdu M. A new shear deformation theory for laminated composite plates. Compos Struct 2009;89:94–101.
[54] Hwu C. Anisotropic elastic plates; 2010.
[55] Hu K-M, Zhang W-M, Peng Z-K, Meng G. Transverse vibrations of mixed-mode cracked nanobeams with surface effect. J Vib Acoust 2016;138.
[56] Engholm M, Pedersen T, Thomsen EV. Modeling of plates with multiple anisotropic layers and residual stress. Sens Actuators, A 2016;240:70–9.
[57] Munir J, Ain Q, Lee HJ. Reliability issue related to dielectric charging in capacitive micromachined ultrasonic transducers: a review. Microelectron Reliab 2019;92:155–67.
[58] Stephen. Theory of plates and shells; 1959.
[59] Carrera EJAMR. In: Ventsel E, Krauthammer T (Eds.), Thin plates and shells: theory, analysis, and applications, vol. 55; 2001. p. 1813–31.
[60] Guo J, Chen J, Pan E. Analytical three-dimensional solutions of anisotropic multilayered composite plates with modified couple-stress effect. Compos Struct 2016;153:321–31.
[61] Tsiatas GC. A new Kirchhoff plate model based on a modified couple stress theory. Int J Solids Struct 2009;46:2757–64.
[62] Chen W, Xu M, Li L. A model of composite laminated Reddy plate based on new modified couple stress theory. Compos Struct 2012;94:2143–56.
[63] Chen W, Li X. A new modified couple stress theory for anisotropic elasticity and microscale laminated Kirchhoff plate model. Arch Appl Mech 2013;84:323–41.